Title: Strong, Rapid and Reversible Photochromic Response of Nb doped TiO_2 Nanocrystal Colloids in Hole Scavenging Media

Authors: Raivis Eglītis,[a] Urmas Joost,[b] Anzelms Zukuls,[a] Kristaps Rubenis,[c] Reinis Ignatāns,[d] Līga Avotiņa,[e] Larisa Baumane,[f] Krisjānis Šmits,[g] Mika Hirsimäki,[h] Tanel Käämbre,[a,b] Andris Šutka [a,b*]

[a] Research Laboratory of Functional Materials Technologies, Faculty of Materials Science and Applied Chemistry, Riga Technical University, Paula Valdena 3/7, Riga, LV-1048, Latvia

[b] Institute of Physics, University of Tartu, W. Ostwaldi Street 1, Tartu, EE-50411, Estonia

[c] Rudolfs Cimdins Riga Biomaterials Innovations and Development Centre of RTU, Institute of General Chemical Engineering, Faculty of Materials Science, Riga Technical University, Pulka 3, Riga, LV-1007, Latvia

[d] Institute of Materials, École polytechnique fédérale de Lausanne, Lausanne, CH-1015, Switzerland

[e] Institute of Chemical Physics, University of Latvia, Jelgavas street 1, Riga, LV-1586, Latvia

[f] Latvian Institute of Organic Synthesis, Aizkraukles street 21, Riga, LV-1006, Latvia

[g] Institute of Solid State Physics, University of Latvia, Kengaraga street 8, Riga, LV-1063, Latvia

[h] Surface Science Group, Faculty of Engineering and Natural Sciences, Tampere University, P.O. BOX 692, FI-33014 Tampere, Finland

Corresponding author: andris.sutka@rtu.lv

Abstract

Understanding photochromicity is essential for developing new means of modulating the optical properties and optical response of materials. Here, we report on the synthesis and exciting new

photochromic behavior of Nb^{5+} doped TiO_2 nanoparticle colloids (NCs). We find that in hole scavenging media, Nb^{5+} doping significantly improves the photochromic response time of TiO_2 nanoparticles. In the infrared regime, Nb-doped TiO_2 NCs exhibit an order of magnitude faster photoresponse kinetics than the pristine TiO_2. Enhanced photochromic response is observed in the visible light regime as well. The transmittance of Nb-doped TiO_2 NCs drops to 10% in less than 2 minutes when irradiated by UV-light in 500 nm range. The photochromic reaction is fully reversible. The physical origin of the high reaction rate is the high Nb^{5+} concentration. As a donor dopant, Nb^{5+} builds up a significant positive charge in the material, which leads to highly efficient electron accumulation during the UV irradiation and results in a rapid photoresponse. EPR experiments identify a new defect type from Nb^{5+} doping, which alters the physical mechanisms available for transmittance modulation. Our new NCs are economic to synthesize and highly suitable for switchable photochromic applications, e.g. smart windows for modulating visible light and infrared transmittance in built-environments.

Keywords: Nb-doped TiO_2; Quantum dots; Photochromic; Photodoping; XPS; Raman; EPR; Nanoclusters

Introduction

Photochromic materials have been proposed for developing new light-based technologies such as smart windows, displays, optical storage media, optical signal processing, and chemical sensors.[1] A plethora of organic, inorganic and organic-inorganic hybrid photochromic materials are known.[2–4] Transition metal oxide (TMO) based inorganic photochromic materials are more extensively studied due to limited stability of organic photochromic materials,[5] as well as due to the high cost of photochromic

materials based on inorganic metal halides and rare earth metals. TMO photochromic materials include nickel oxide (NiO),[6] tungsten oxide (WO_3),[7–11] molybdenum oxide (MoO_3),[12–15] vanadium oxide (V_2O_5),[16] niobium oxide (Nb_2O_5),[17] and titanium oxide (TiO_2).[18,19] Even though they are more stable and cost effective than organic, metal halide and/or rare earth based photochromic materials, most TMO photochromic materials do not meet the requirements of sustainability and environmental safety. For example, W and V are scarce elements with a supply risk,[20] and Ni is associated with environmental and health risks potentially making the use of Ni in photochromic devices un-attractive. ZnO nanomaterials, in turn, have stability issues. They are prone to photocorrosion[21] and can recrystallize in presence of humidity in ambient atmosphere conditions.[22]

In contrast, Titanium dioxide (TiO_2) is an earth-abundant, non-toxic and chemically stable wide band gap semiconductor. As a proven photo(electro)catalytic material, its properties and applications have been extensively investigated.[23] The light-induced chemical reactions on the TiO_2 surface can be harnessed as a means of photodoping[24] the material and, consequently, modulating the transmittance of TiO_2 particle suspensions[25] or even thin films.[26] For instance, TiO_2 nanoparticles have been previously mixed in PVA matrix to observe a photochromic response.[27,28] The hydroxyl -OH groups on PVA were found to act as photogenerated hole scavengers,[29–31] thus allowing photogenerated electrons to populate the conduction band and, in turn, modulate the optical properties of the material. However, in Degussa P25 TiO_2/PVA systems, the observed reduction in the transmission of light was only about 20%.[32]

In our recent paper, we reported on the properties of a highly responsive photochromic colloidal system consisting of ultrafine TiO_2 nanoparticle in butanol,[24] with the butanol acting as a strong photogenerated hole scavenger.[33] Utilizing ultrafine nanoparticles with an average diameter smaller than 5 nm allowed us to significantly reduce light scattering in the suspension and to maximize the initial transmittance. We observed that upon UV irradiation the system's transmittance decreased to 0% within

60 minutes. More importantly, the optical properties of our colloids were modulated in a near-uniform manner across a broad wavelength range. Significant absorption was observed from the visible to near-infrared region, and even to thermal black body radiation regime. We have also shown, that for un-doped TiO_2, changing the surrounding medium (solvent) as well as adding hole-scavenging additives can increase the photochromic response.[34]

We now estimate that approximately 50 μm thick layer consisting of our photochromic TiO_2 nanoparticles would be sufficient to allow a windowpane to become opaque to both visible and mid-infrared light. However, the photochromic response time of about 60 min in our previously reported TiO_2/butanol system[24] is clearly insufficient for it to be competitive in demanding smart windows applications. In comparison, WO_3 ultrafine nanoparticle suspensions in ethylene glycol exhibit a much faster response time (10 s) upon exposure to solar light.[20]

To address the observed slow reaction kinetics, we turn our focus on Nb-doped TiO_2. This class of materials has received scientific and technological interest due to its promising electrical and optical properties.[35] It has been proposed not only as a potential low-cost alternative to such popular transparent conducting oxides as Sn-doped In_2O_3[36] and F-doped SnO_2[37], but also as a key to improved dye-sensitized solar cells[38] and for applications in photocatalysis.[23] The attractive properties of Nb-doped TiO_2 nanoparticle colloids (NCs) stem from their tunable electronic structure. They exhibit a localized surface plasmon resonance that strongly couples the energy of the incoming photons to the electronic structure of the colloid particles.[39] The plasmon resonance itself can be tailored for different applications by varying the Nb dopant concentration, thus enhancing the versatility of Nb-doped TiO_2 NCs as a photonic material.

The photochromic response in pristine TiO_2 is well-known to produce oxygen vacancies with accompanying Ti^{3+} ions. The excess electrons created are associated with intrinsic donor defects where

they fill new electronic states that exist ~0.1 eV below the conduction band minimum.[40] In contrast, by doping TiO_2 with Nb^{5+} (as a substitution for Ti^{4+}), the resulting crystal lattice will exhibit Nb^{5+}-Ti^{3+} defect pairs. There is also a concomitant shift both in the position of the Fermi level and the conduction band minimum.[41] Furthermore, Nb^{5+} doping has shown to reduce the number of oxygen vacancies[42] and suppress the charge recombination rate at the TiO_2 surface.[43]

In this work, we present *an economic two-step high-yield method for colloidal synthesis of Nb-doped TiO_2 NCs.* NCs investigated in the present work exhibit a size distribution (diameter) range from 3.6 nm to 6.7 nm. Maximum Nb doping level (Nb/Ti) of 19.8 % was attained. We find that in the infrared regime, our Nb doped system exhibits an order of magnitude faster photoresponse kinetics than the pristine TiO_2. In the visible light regime, the transmittance of Nb-doped TiO_2 NCs is reduced to 10% in less than 2 minutes when irradiated by UVA-light (365 nm) in 500 nm range. Steady-state experiments indicate that the observed photochromic reaction is also reversible. Finally, we discuss the enhanced performance of the doped TiO_2 NCs in terms of Nb-induced changes in the electronic and defect structure of TiO_2.

Material and methods

Particle synthesis and sample preparation

The particles were synthesized using a synthesis route first described by *Scolan* and *Sanchez*[44] and modified by us for the preparation of Nb doped TiO_2. The procedure was as follows: titanium tetra *n*-butoxide (97%, Sigma-Aldrich) was added dropwise to a mixture of acetylacetone (≥99.0%, Merck) and *n*-Butanol (≥99.5%, Merck) at room temperature while stirring under nitrogen flow. In parallel, niobium (V) ethoxide was added dropwise to a mixture of acetylacetone and *n*-Butanol while stirring under

nitrogen flow. After 10 min, the niobium precursor solution was added dropwise to the titanium precursor solution. After 15 min, a solution of 4-dodecylbenzene sulfonic acid (4-DDBSA, ≥95%, Sigma-Aldrich) and de-ionized (DI) water was added dropwise to the mixture. The resulting mixture was then heated up to reflux and kept at reflux for 12 hours. After that, the mixture was transferred to a Teflon autoclave and kept at 150 °C for 24 h. Subsequently, the mixture is cooled down to room temperature, during which we observed formation of a yellowish precipitate. The precipitate is then centrifuged at 2000 g for 1 h, washed twice with methanol and centrifuged at 4000 g for 1 h. The final paste is initially dissolved in a small amount of *n*-butanol and then diluted in order to get a concentration of 100 g/L. The surfactant to particle ratio was 20 % by weight. The synthesis yield is 84.5-85% depending on the amount of Nb present. These colloids have been found to remain stable (stabilized manly by the 4-dodecylbenzene sulphonic acid on the particles) at room temperature without sedimentation even for years.

Sample characterization

The particles were characterized by x-ray diffraction XRD (*PANalytical X'Pert*), Raman spectroscopy (*Renishaw inVia*) and transmission electron microscopy (*TEM, Tecnai G20, FEI*) imaging at 200 kV. Sample selected area electron diffraction imaging (SAED) was performed. The samples for TEM analysis were placed on a perforated carbon film on 400 mesh copper grid (Agar Scientific S147-4). Rietveld refinement was done in order to evaluate the grain size and unit cell dimensions, using Profex software.[45] The particle size distribution was determined using ImageJ software.[46] To evaluate the photochromic performance of the particle colloids with different Nb content, 3.0 mL of the test solution with a particle concentration of 100 g/L were transferred into a UV-quartz macro cuvette. The cuvette was sealed with a LD-PE cap and epoxy resin with an inlet for air and an outlet for pressure

equalization. The test solution was irradiated using a triple UV-LED setup with a wavelength of 365 nm and a light intensity of 15 mW/cm^2 (experimental setup diagram can be found in ESI Fig. S1). The UV-Vis spectra were acquired using a *TermoScientific Genesys 10S* UV-Vis spectrometer.

To observe the decoloration of the photodoped NP colloids, two different recovery experiments were carried out: dynamic and steady state. In the dynamic experiment, air was injected into the irradiated samples at a rate of 1.0 mL/min. After each dose (1.0 mL) of air, UV-Vis spectra were acquired for the sample. Air exposure-measurement cycles were conducted until there was no discernable change in the spectroscopically determined transmittance, or the cumulative dose of air reached 20.00 mL. In the steady state experiments, 5.0 mL of air was injected into the irradiated samples and the transmittance was determined every 10 minutes via spectroscopy. The experiment concluded when no change in transmittance could be observed.

The charge carrier concentration was determined by utilizing the method used previously by Schimpf et al.[47] for ZnO NCs and by us for the charge carrier concentration determination for TiO_2 NCs.[24] Titration for the purpose of charge carrier determination was carried out by diluting the initial suspension to 2 g/L and irradiating the sample until no change in the absorbance spectra was noticeable. This was followed by injecting specific amounts of a *n*-butanol solution of iron (III) acetylacetonate into the cuvette, waiting 30 seconds and then measuring the resulting Vis spectra of the solution with a UV-Vis spectrometer. To compare how the absolute change in transmittance varies between NCs as a function of synthesis parameters, the transmittance of the diluted (2 g/L) samples was measured for every NC and $\Delta T\%$ (absolute change in transmittance) was determined from these spectra.

Electron paramagnetic resonance (EPR) spectra were acquired for unirradiated and irradiated colloids using an X-band spectrometer (*Bruker EMX-plus*) with a microwave frequency of 9.86 GHz and power of 20 mW, magnetic field sweep width of 400 G with a center at 3540.0 G, a receiver

modulation frequency of 100.0 kHz with an amplitude of 5.00 G, and a receiver gain of 1×10^4 at room temperature. The colloids were transferred into 50 µL capillaries with an internal diameter of 1.0 mm and subsequently irradiated with the triple UV-LED array. The amount of radicals present in a sample was calculated by comparing the second integral of the sample signal to a standard known to contain 1.15×10^{-3} % spins.

The X-ray photoelectron spectra (XPS) were acquired using a *Scienta SES100* hemispherical analyzer and a non-monochromatized Mg-Kα radiation source (a *Thermo VG Scientific XR-4* dual anode X-ray gun), with a resulting overall resolution of approximately 0.7 eV. The binding energy scale of the slightly charging sample was corrected by fixing the C 1s peak of adventitious carbon to 284.8 eV. The XPS sample was prepared by pressing a ground sample powder into indium foil.

The Nb/Ti relative content was evaluated using *CasaXPS* software, comparing the XPS spectral areas (after subtracting Tougaard background) of Ti 2p and Nb 3d peaks and considering the individual photoionization cross sections, inelastic mean free path, and the spectrometer transmission function.

Diffuse reflectance measurement for Kubelka-Munk plots and band gap calculation was carried out using a *Shimadzu SolidSpec UV-3700* spectrometer with an integral sphere in the wavelength range of 300-1600 nm.

Results and discussion

Particle characterization

According to XRD, Raman as well as SAED, the particles consist of the anatase crystalline phase (JCPDS 21-1272).[48] The doping with Nb^{5+} didn't cause any secondary phase segregation. The Raman peaks in Figure 1 A at 152, 402, 516 and 642 cm^{-1} can be attributed to the E_g, B_{1g}, $A_{1g}+B_{1g}$ and E_g

modes, respectively.[49] There is a slight increase in the width of the main E_g peak at 152 cm^{-1} in increasing Nb^{5+} content. This has been attributed to the formation of Nb-O-Ti bonds.[41] The peak itself is slightly red shifted comparing to bulk TiO_2 due to the sufficiently small size of the particles.[50] There is also an increase in the intensity of the second E_g mode peak at 642 cm^{-1}, further confirming the presence of Nb-O bonds.[51] The slight shift of this peak to lower wavenumbers correlates well with the change in the crystallite size, which is confirmed also by Rietveld refinement studies and TEM imaging. The shift of the B_{1g} mode peak at 402 cm^{-1} with increasing Nb^{5+} content is another confirmation as successful Nb^{5+} incorporation in the TiO_2 crystalline lattice, as this mode stems from the Ti-O bond stretching.[52] The broad peak at 920 cm^{-1} can be attributed to O-O stretching vibration, that can stem from excess oxygen in the crystalline lattice.[53,54]

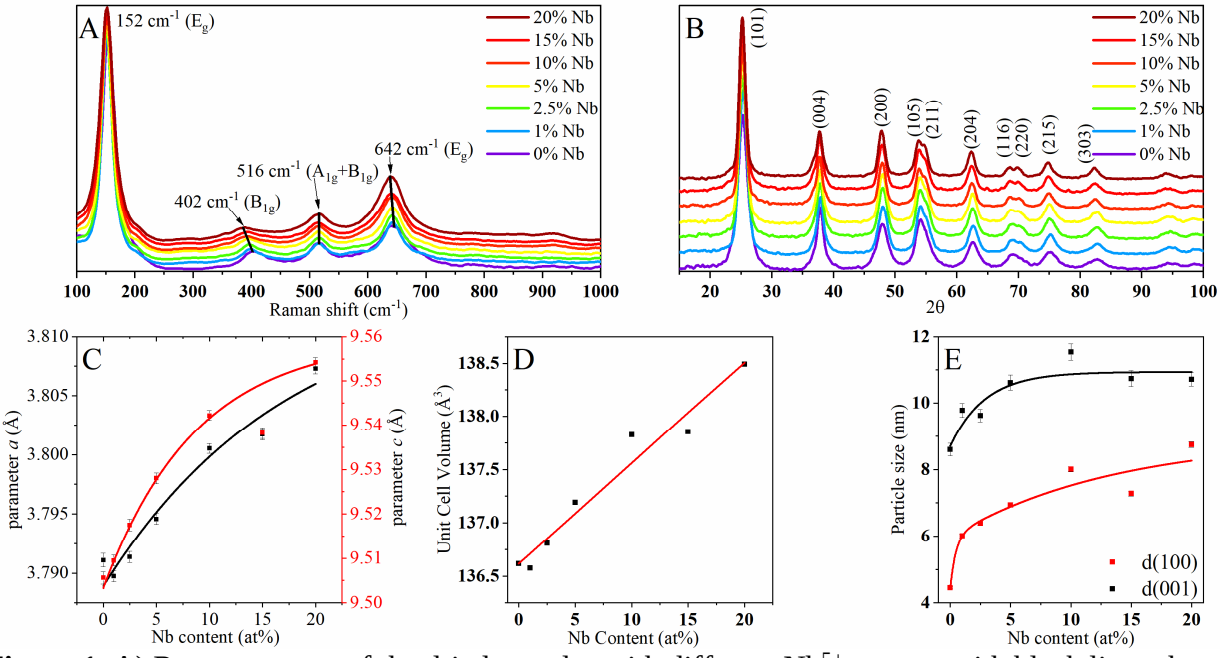

Figure.1. A) Raman spectra of the dried samples with different Nb^{5+} content with black lines showing a peak shift with increasing Nb content for peaks at 402.5 and 644 cm^{-1}. B) XRD results of the dried samples with different Nb content; C) *a* and *c* unit cell parameter change with increasing Nb^{5+} content with lines indicating an exponential fit for both *a* and *c* parameters. D) Unit cell volume dependence on the Nb content with the red line indicating a linear correlation between cell volume and Nb^{5+} content. E) Grain size width-wise (d(001)) and length-wise (d(100)) with exponential fits for both parameters.

XRD results as seen in Figure 1 B are in good alignment with the results from our previous investigation. There is a slight shift in the (101) diffraction peak from 25.305 to 25.188. This is indicative of increased lattice plane spacing[50] that stems from the incorporation of slightly larger Nb^{5+} (0.78 Å) as compared to Ti^{4+} (0.75 Å).[55] The Rietveld refinement results shown in Fig.1C-E further elaborate these observations. The *a* and *c* parameters of the anatase unit cell increase exponentially with the Nb^{5+} content (see Figure 1 C). The *a* parameter grows from 3.791 Å for the un-doped TiO_2 NCs to 3.807 Å for the sample with 20% Nb^{5+} content. A similar growing trend was observed for the *c* parameter that showed an increase from 9.506 Å to 9.554 Å. As a result, the unit cell volume increases from 136.618 $Å^3$ to 138.493 $Å^3$ (see Figure 1 D).

Due to the increase in the unit cell volume, the size of the crystallite grows in the direction of both *a* and *c* axes (see Figure 1 E) as a function of Nb^{5+} content. However, the observed growth is not isotropic as the particles transform from an initially spherical shape to slightly more elliptical crystallites. The increase in crystallite size as well as change in the shape is clearly confirmed in TEM images (see Figure 2 A-G) that are in a good agreement with the XRD data. Another insight gained from the SAED diffractograms is that individual crystalline nanoparticles are single crystals. The observed anatase diffraction fringes are a result of multiple particles contributing to the SAED spectra and they correspond to reflection from (101), (004), (200), (105), (204), (220) and (215) planes[56] (see Figure 2 H-I). The average particle size d(50), as determined from the TEM images, increased from 3.58 nm to 6.67 nm for un-doped TiO_2 NCs and the sample with 20% Nb content (see ESI Figure S2), respectively. It can also be seen from the TEM images, that the particles are crystalline throughout, without any hints at a core-shell structure as seen in ESI Figure S3.

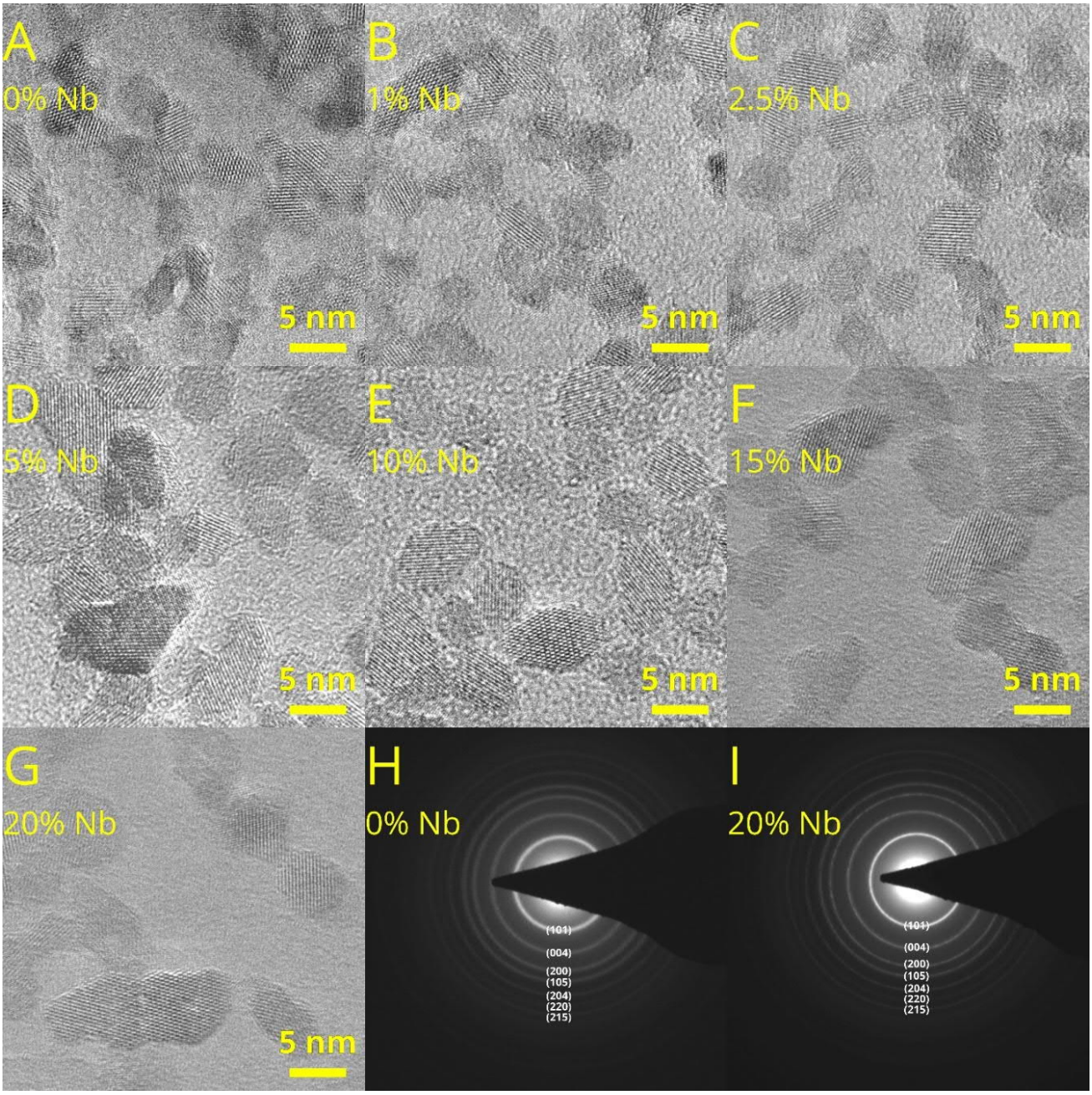

Figure.2. A-G) High resolution TEM images of the synthesized particles with different Nb content. H and I) Selected Area Electron Diffraction Pattern for pure TiO_2 and TiO_2 with 20% Nb^{5+}.

The band gap was calculated from the diffuse reflectance spectra (see ESI Figure S4 A and B). According to our analysis, the optical band gap decreases gradually with increasing Nb content. As shown in ESI Figure S4 A, the band gap can be tuned from 3.13 eV for the un-doped TiO_2 to 2.98 eV for the sample with 20% Nb^{5+} (see ESI Figure S4 B). The observed shrinking of the band gap can be

attributed to lattice point defects and formation of additional absorption states in TiO_2 band gap.[57] In accordance with known defect chemistry, Nb^{5+} doping likely produces several different types of point defects (eq. 1-5):

$$Nb_2O_5 \xrightarrow{TiO_2} 2Nb_{Ti}^{\bullet} + 5O_O^x + V_{Ti}'''' + V_O^{\bullet\bullet} \quad (1)$$

$$2Nb_2O_5 \xrightarrow{TiO_2} 4Nb_{Ti}^{\bullet} + 10O_O^x + V_{Ti}'''' \quad (2)$$

$$Nb_2O_5 \xrightarrow{TiO_2} Nb_{Ti}^{\bullet} + 4O_O^x + O_i'' \quad (3)$$

$$Nb_2O_5 \xrightarrow{TiO_2} 2Nb_{Ti}^{\bullet} + 4O_O^x + \frac{1}{2}O_2 + 2e^- \quad (4)$$

$$Nb_2O_5 \xrightarrow{TiO_2} 2Nb_{Ti}^{\bullet} + 4O_O^x + 2Ti^{3+\prime}{}_{Ti^{4+}} + \frac{1}{2}O_2 \quad (5)$$

The oxygen vacancies create new donor levels between 0.75 eV and 1.18 eV below the conduction band,[58] the Ti^{4+} vacancy introduces an acceptor level 1.15 eV above valence band edge,[59] and the Ti^{3+} creates shallow donor levels slightly below conduction band minimum.[58] These point defects can contribute to the apparent narrowing of the band-gap. The observed shrinking of the band gap is in sharp contrast with the work published by Trizio et al., where the TiO_2 doping by Nb^{5+} causes the band gap widening due to Moss-Burstein effect.[60] The differences between the present study and the study reported by Trizio et al. can be related to different compensation mechanism for excess charge introduced by donor Nb^{5+} dopant. The Moss-Burstein effect is widely observed when the excess positive charge is compensated by delocalized electron in conduction band forming degenerated semiconductor. As the delocalized electrons are occupying the first levels in the conduction band, the higher energy is needed to excite electrons from lowest occupied level in valence band to unoccupied level in conduction band. In the present work the excess charge from Nb^{5+} is most likely compensated by means of other point defects such as oxygen interstitials or Ti vacancies.

The incorporation of Nb into TiO_2 NCs was investigated by X-ray photoelectron spectroscopy (XPS). Figure 3 shows XPS scans over the Ti 2p, Nb 3d and O 1s region. The binding energies and spectral features of the photopeaks are repeatable throughout the series. As expected, only the relative spectral weight of Nb 3d relative to Ti 2p varies with Nb^{5+} concentration, and it does so in an excellent agreement with the nominal synthesis values (Table 1). In general, the level of agreement between the nominal and the measured values for Nb^{5+} concentration indicates that, at least in the investigated concentration range, there are no relevant kinetic barriers to doping, and that our synthesis technique is very efficient at incorporating Nb into TiO_2.

The chemical states of Ti and Nb were resolved from the XPS spectral features (full spectrum available in ESI Figure S5). The binding energy of the Ti 2p 3/2 peak at 458.5 eV indicates a homogeneous Ti^{4+} oxidation state, and the Nb 3d 5/2 peak at just above 207 eV indicates Nb^{5+}. The O 1s spectrum with its relatively sharp peak at slightly below 530 eV binding energy corresponds to lattice oxygen in bulk oxide, while the shoulder above 531 eV, usually attributed to (surface) hydroxide species and/or adjacent oxygen vacancy sites, appears as a very weak signal.

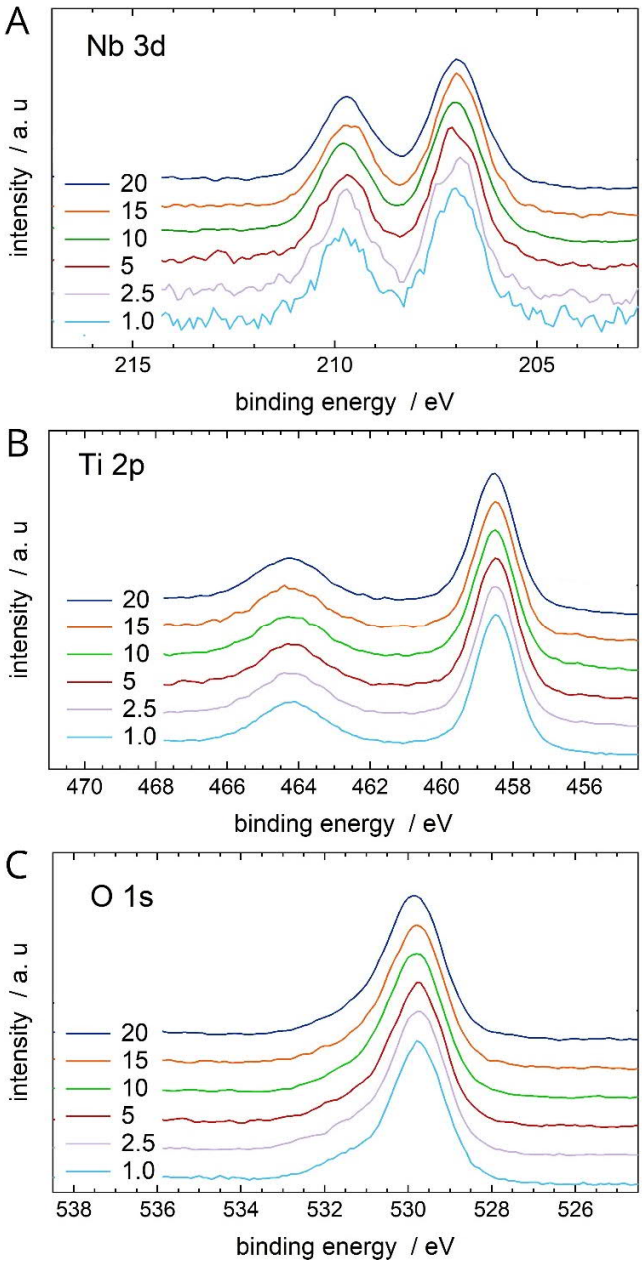

Figure.3. XPS spectra of Nb-doped TiO_2 NCs showing: A) Nb 3d; B) Ti 2p; C) O 1s.

Table 1. Nb content in the particles as determined by XPS versus nominal values in synthesis

Nb content in synthesis (mol%)	Nb content in particles according to XPS (mol%)
1	1.1±0.2
2.5	2.6±0.2
5	5.4±0.2
10	10.1±0.2

15	14.8±0.2
20	19.9±0.2

Photochromic properties

For photochromism tests, the samples were dispersed in butanol with a particle concentration of 100 g/L and irradiated by UV light. Transmittance change versus time plots were recorded to study the photochromic response kinetics. Initially the nanoparticle colloids show full transmittance in the visible and infrared range, whereas in the study reported by Trizio et al.,[37] Nb doped TiO_2 nanocrystals show plasmonic absorption peaks starting at about 500 nm. This again confirms, that the compensation mechanism of the excess charge introduced by donor Nb^{5+} dopant is different for the materials reported here, perhaps, due to the different synthesis conditions. It is important to add also that the initial transmittance for Nb^{5+} doped TiO_2 nanoparticle colloids decreases by 0-18%, depending on the wavelength as can be seen in ESI Figure S6. This effect can't be related to slight increase in nanoparticle size because even larger Nb doped TiO_2 nanoparticle colloids reported by De Trizio et al. do not show any scattering effects. The observed decrease of initial transmittance for Nb doped TiO_2 nanoparticle colloids thus has to be related to aggregation and, consequently, to the formation of scattering centers, creating a slightly opaque effect. Upon UV irradiation all samples exhibit notable photochromic response (decrease in transmittance) in the measured wavelength range (400-1100 nm) (ESI Figure S6) and can be cycled between photodoped and recovered state (ESI Figure S7). The observed changes in transmittance can be related to combined effects of midbandgap level formation and itinerant electron accumulation in the conduction band.[24] When TiO_2 is irradiated with UV light, electron and hole pairs are formed (6). Holes are scavenged by the butanol (7), but electrons accumulate in the conduction band or participate in the reduction of Ti^{4+} to Ti^{3+} (8), thereby producing oxygen vacancies V_O (9). In the presence of Nb^{5+} the electrons also facilitate the reduction of Nb^{5+} to Nb^{4+} (10):

$$TiO_2 + hv \rightarrow e'_{CB} + h^{\bullet}_{vb} \quad (6)$$

$$h^{\bullet}_{vb} + OHCH_2R \rightarrow H^+ + R\dot{C}HOH \quad (7)$$

$$e'_{CB} + Ti^{4+} \rightarrow Ti^{3+} \quad (8)$$

$$Ti_2O_3 \xrightarrow{TiO_2} 2Ti(III)'_{Ti(IV)} + 3O^x_O + V^{\bullet\bullet}_O \quad (9)$$

$$Nb^{5+} + e'_{CB} \rightarrow Nb^{4+} \quad (10)$$

The photoresponse kinetics were observed to accelerate with increasing Nb^{5+} concentration. NCs from TiO_2 with 20% of Nb^{5+} showed a transmittance of 10% after only 2 min of irradiation at 500 nm (see ESI Figure S6 G). In comparison, pristine TiO_2 nanoparticle colloidal suspensions attained the same transmittance after 15 min (see ESI Figure S6 A).

To understand how the photoresponse for different nanoparticle colloids (Figure 4 A) is changing at different wavelength ranges, the rate of change in transmittance during the UVA irradiation was calculated from T/T_0 plots (ESI Figure S8). The transmittance change kinetics at short wavelengths (420-450 nm) are relatively independent of the Nb content of the colloid. At wavelength range 500-700 nm, the T/T_0 kinetics exhibit more sensitivity to the nanoparticle composition than in short wavelengths. Finally, in the NIR range (700-1100 nm), there is nearly a tenfold increase in the reaction rate constant k as the Nb content is increased from 0% to 20%. Of course, nanoparticle size can also influence the response, as the hole scavenging and as such, the photodoping, is surface size dependent. However, an increase in particle size (reduction in surface area by about 50% when comparing un-doped TiO_2 to 20% Nb-doped TiO_2) would hamper the photochromic response rate.

In NIR range, the modulation of transmittance has been previously attributed to plasmonic oscillations of photogenerated electrons in conduction band,[39] while the absorption in visible regime is due to formation of additional absorption levels in the TiO_2 band gap. The origin of such energy levels

can be plausibly assigned to lattice defects (such as oxygen vacancies) and Ti^{3+} sites the both of which are capable of compensating (localizing) the photogenerated excess electrons.[24]

To understand the role of Nb doping, it is useful to compare the wavelength dependence of the photoresponse kinetics for pristine TiO_2 and the Nb-doped TiO_2. For the former, the reaction rate shows only weak differences in the various wavelength ranges – the rate constant is 0.123 min^{-1} at 450 nm and 0.247 min^{-1} at 1000 nm. In contrast, the rate constant for Nb^{5+} doped TiO_2 NCs grows by an order of magnitude in the investigated wavelength range. For the sample with 20% of Nb^{5+} the rate constant is 0.155 min^{-1} at 450 nm and 3.195 min^{-1} at 1000 nm. This significantly faster reaction rate facilitating absorption for Nb-TiO_2 in the infrared region (while irradiating with UV-light) strongly indicates that Nb^{5+} reduces the recombination rate and facilitates more efficient accumulation of itinerant electrons in the conduction band. This can be attributed to the excess positive charge from Nb^{5+} donor dopant in TiO_2 that impart the extra accumulation capacity of electrons in conduction band.[37,39]

In order for our NC to be a suitable candidate material for photochromic infrared switchable smart window devices, the photochromic reaction must also be reversible. In the dynamic recovery experiment (spectra in ESI Figure S9 A and T/T_0 plots in ESI Figure S10 A), the un-doped TiO_2 sample required only 4.0 mL of air to revert almost back to its initial transmittance. However, the recovery is not complete. We see a noticeable drop in transmittance in the 400-600 nm range. It is reasonable to attribute this residual dip to sub-surface Ti^{3+} defects and V_O the both of which are more persistent than the delocalized electrons responsible for the absorption in NIR.

Doping TiO_2 NCs with Nb strongly influences the recovery process. The sample with 1% Nb required an air exposure between 5 and 6 mL in order to revert close to its initial transmittance value (ESI Figure S10 B). With increasing Nb content, the reverse reaction becomes slower and slower. The

sample with 20% Nb did not show significant reaction to air. This is reflected also in the transmittance change rate constants in Figure 4B.

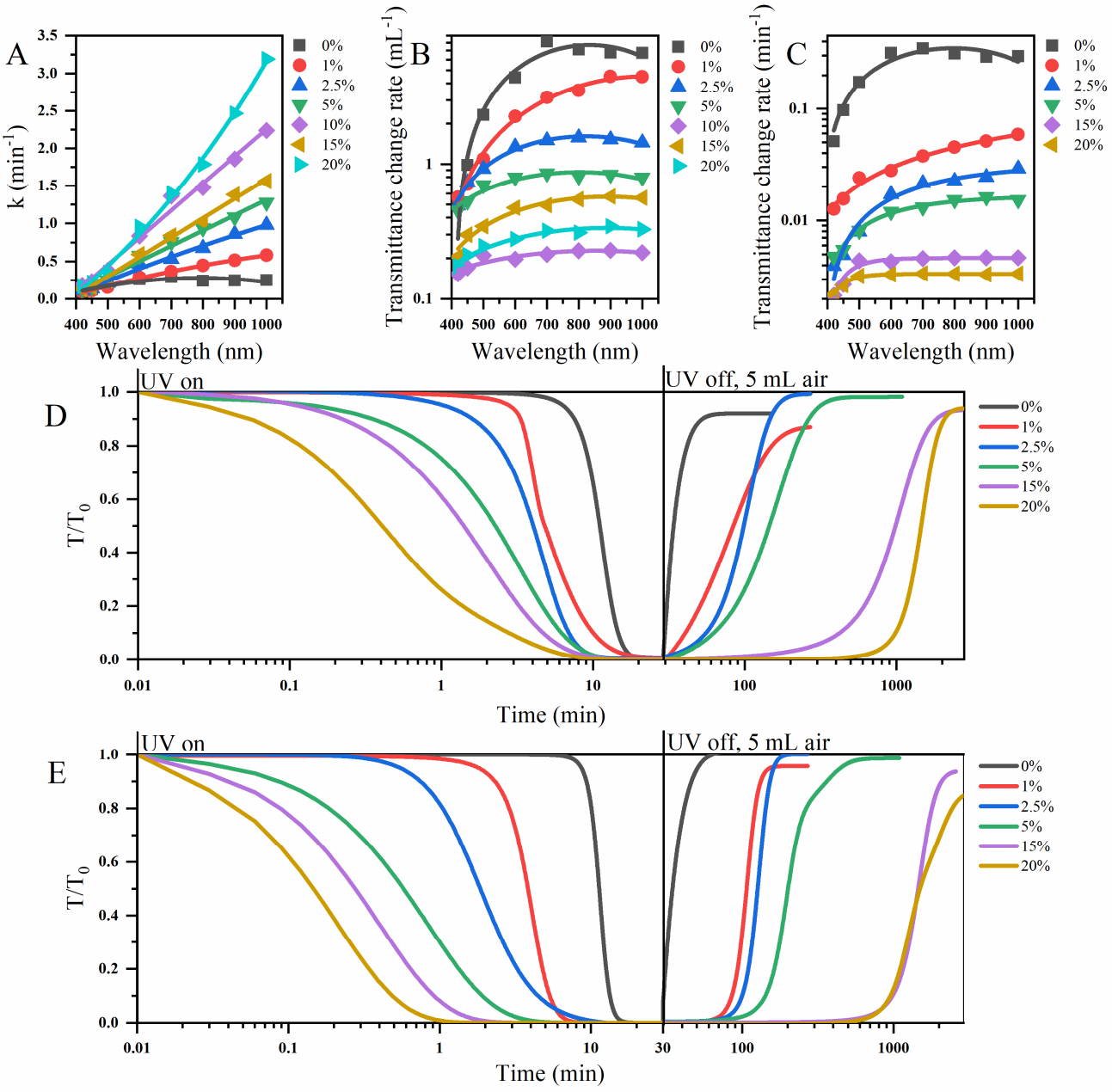

Figure 4. Time constant k for A) the photochromic response to UV irradiation of undoped and Nb-doped TiO_2 NPs suspensions at different wavelengths and with different Nb content; B) dynamic recovery experiment with continuous air injection of undoped and Nb-doped TiO_2 NPs suspensions at different wavelengths and with different Nb^{5+} content; C) steady state recovery with only 5 mL of air injected for undoped and Nb-doped TiO_2 NPs suspensions at different wavelengths and with different Nb^{5+} content; D) UV photoresponse and steady state recovery transmission curves for samples with

different Nb content at 550 nm; E) UV photoresponse and steady state recovery transmission curves for samples with different Nb content at 1000 nm;

In steady state recovery experiments, the change in transmittance was recorded after injecting 5 ml of air (Figure 4 D and E for values at 550 nm and 1000 nm respectively, see ESI Fig. S11 for other wavelengths). The recorded time to recovery varied from 20 min for the pristine TiO_2 to 45 hours for the sample with 20% Nb. This is also evident from the time constants depicted in Figure 4C. The slow recovery of Nb doped TiO_2 indicates that the delocalized electrons are strongly stabilized by the extra positive charge gained from Nb^{5+}. All samples show slower recovery in visible range than in infrared range, because delocalized electrons have less affinity towards participating in oxidation reactions than electrons localized by Ti^{3+} or Nb^{4+}-V_O-Ti^{4+}.[61] Hence, the low transmittance state of Nb-TiO_2 NCs is exceptionally stable.

Faster recovery of the optical properties for 20% Nb-doped TiO_2 colloid can be achieved by adding 25 mol% of triethanolamine (TEA, calculated relative to the amount of Nb-doped TiO_2). The addition of TEA increased the recovery rate from 0.0008 min^{-1} to 0.036 min^{-1} (at 1000 nm) without the air injection (for T/T_0 plots and transmittance change rate graphs, see ESI Figure S12). The initial transmittance for 20% Nb-doped TiO_2 nanoparticle colloid containing TEA additive is restoring in 360 minutes, while by 5 ml air injecting (without the TEA) recovery took 1080 minutes. The recovery of the initial transmittance in the presence of TEA can be related to the electron scavenging by TEA oxidation products produced by photogenerated holes.[62] A detailed study of the impact of TEA on photochromic response and recovery properties will be reported elsewhere in near future.

The absolute change in transmittance was compared for colloids diluted to a concentration of 2 g/L and UV irradiated for 24 h. The transmittance at 550 nm before and after irradiation is shown in Figure 5A and the corresponding transmittance spectra for various sample colloids are demonstrated in

ESI Figure S14. The absolute change in transmittance at 550 nm correlates well with the amount of Nb^{5+} in the particles ranging from 40% for un-doped TiO_2 colloid to 8% for the colloid with 20% Nb^{5+}.

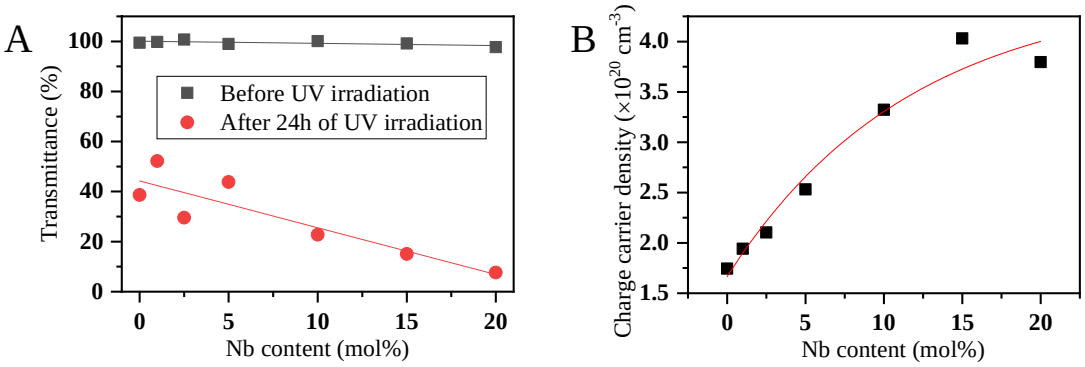

Figure.5. A) Transmittance at 550 nm before and after 24 h irradiation for samples with a colloid concentration of 2 g/L; B) Charge carrier concentration, determined via redox titration.

Titration experiments were then conducted on the same suspensions in order to estimate the charge carrier concentration in nanocrystals. According to our titration results, the NCs - when photodoped to saturation - had a charge carrier concentration of 1.74×10^{20} cm^{-3} for the un-doped TiO_2. The charge carrier concentration increased to as high as 4.03×10^{20} cm^{-3} when the Nb^{5+} content in NC was increased to 20% (see Fig. 5B). Charge carrier concentrations of this magnitude have been previously reported for both NCs when they have been doped electrochemically.[39] This shows, that doping with Nb^{5+} imparts extra accumulation capacity, allowing a higher number of charge carriers.

To gain deeper insights into the photochromic behavior of undoped and Nb^{5+} doped TiO_2, we investigated the band gap size during UV irradiation by optical absorbance measurements using integrated sphere (see Experimental section for details). We found that UV irradiation changed the optical band gap size for both un-doped and Nb^{5+} doped TiO_2. However, Nb-doping had an interesting effect on the sign of the change. First, we observed that the band gap for the un-doped TiO_2 NC colloid increased from 2.86 eV to 2.94 eV during UV irradiation. This is in line with the results obtained in our previous investigation[24] and can be attributed to Moss-Burstein effect.[60] In contrast, the band gap for

TiO_2 containing 20% of Nb^{5+} *decreased* from 2.84 eV to 2.56 eV. This opposite sign of the change indicates that the photodoping produces different type of defects in Nb-TiO_2 than in un-doped TiO_2.

To gain further insights into the defects and to resolve the behavior of the Ti and Nb cations during UV irradiation and recovery, we conducted a set of EPR measurements. Prior to UV irradiation, the un-doped TiO_2 NC exhibited three EPR peaks at a g-value of 2.0238, 2.0098 and 2.0036. They are attributable to Ti^{4+} and O^{2-} just like in our previous experiments.[24] During UV irradiation these three signals are replaced by a new and much more intense signal at a g-value of 1.957 with a line width ΔH=12.9 G, which can be attributed to Ti^{3+}.[63] This signal increased in intensity with irradiation time, reaching a maximum after 60 min of irradiation (see Figure 6 A). The amount of Ti^{3+} corresponding to this signal was calculated by with the help of a standard (Bruker ER 4119HS-2100) with known spin concentration. The maximum Ti^{3+} concentration was determined to be 3.01×10^{-3} % or 1.812×10^{21} spins/mol after 60 min irradiation.

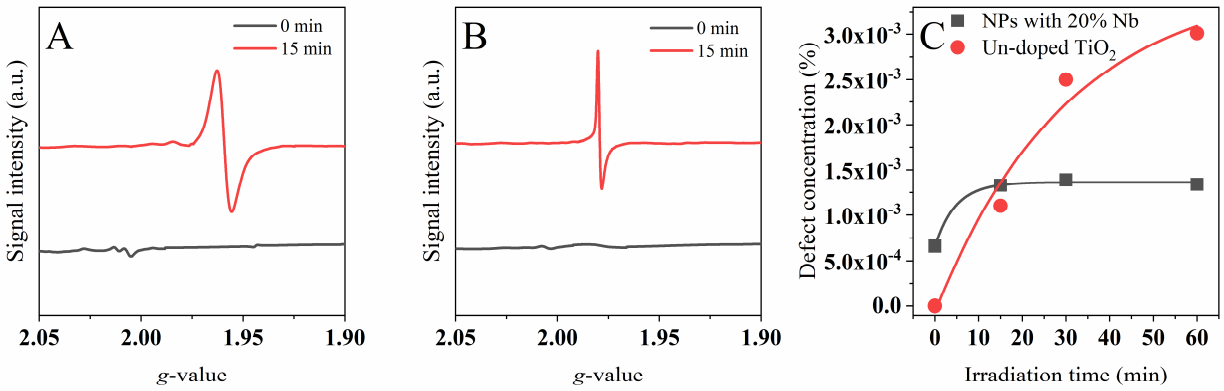

Figure.6. EPR spectra for the un-doped TiO_2 NP colloid (A) and with 20% Nb (B) before irradiation and after 15min of UV irradiation. C) defect concentration (Nb^{4+}-V_O-Ti^{4+}. and Ti^{3+}) as calculated from the EPR spectra (A and B).

Identical EPR experiments were carried out also for an Nb-TiO_2 NC with 20% Nb content (see Figure 6 B). Before UV irradiation, we observe the same three signals as on TiO_2. However, there is no evidence of a Ti^{3+} signal either during and after UV irradiation. Instead, a new spectral feature with a

g-value of 1.977 and ΔH=4G was detected and its intensity was seen to increase with irradiation time. This signal can be attributed to Nb^{4+} to be precise, the defect model of Nb^{4+}-V_O-Ti^{4+}.[61] They describe, that, such a defect configuration can make the signal detectable at temperatures above 77K. The result indicates that for Nb^{5+} doped TiO_2, the main charge compensation mechanism leads to the formation of Nb^{4+}, but also that the compensation mechanism is available only during UV irradiation. Prior to UV irradiation, the initial compensation is due to other point defects. The calculated amount of defects was less than on the un-doped TiO_2 NC, and it reached saturation after 30 min of irradiation instead of 60 min. This observation is in agreement with our UV-Vis spectroscopy results that show a higher transmittance change rate for samples doped with Nb^{5+} (see Figure 6 C).

Conclusions

The synthesis technique reported here yields good quality Nb^{5+} doped anatase TiO_2 NCs. The experimentally obtained dopant concentrations conform well to the nominal values in the synthesis. The observed nanoparticle size shows clear dependence on the Nb concentration and varies from 3.58-6.67 nm. This is due to incorporation of Nb into the lattice structure and the resulting anisotropic unit cell growth cell along the two unit cell axes. Consequently, the shape of NCs change from elliptical to spherical shape as the doping level increases. The optical performance of TiO_2 NCs is strongly enhanced by Nb^{5+} doping. Contrary to pristine TiO_2, Nb^{5+} doped NCs show much more sensitivity to light in the infrared range than in the visible range. We attribute this discovery to a new transmittance modulation mechanism facilitated by the Nb^{5+} dopants. As donors, Nb^{5+} provides excess positive charge in the lattice thus enabling delocalized electron accumulation. During photodoping, Nb^{5+} efficiently localizes photoelectrons by becoming (as indicated by our EPR studies) reduced to form a new defect structure Nb^{4+}-V_O-Ti^{4+}. Together, these two reaction pathways efficiently modulate the Nb-TiO_2 NC's

transmittance and facilitate the observed reversible photochromic response. In summary, our Nb^{5+} doped TiO_2 photochromic materials show great promise for being highly versatile photochromic infrared switchable materials. Upon further optimization of the oxidization mechanism for the reverse reaction (e.g. by introducing chemical additives or electric potential), we believe that our NCs will make excellent materials for e.g. infrared modulating smart window devices and, in general, energy management in built-environments.

Acknowledgements

This work was supported by the Latvian Council of Science in the framework of FLPP (Plasmonic oxide quantum dots for energy saving smart windows, lzp-2018/1-0187). MH acknowledges financial support from the Jane and Aatos Erkko Foundation (SOFUS: Solar Fuel Synthesis – Mitigating the climate change by conversion of carbon dioxide and water into solar fuels). TK acknowledges financial support from TK141 for XPS experiments.

References

(1) Wang, S.; Fan, W.; Liu, Z.; Yu, A.; Jiang, X. Advances on Tungsten Oxide Based Photochromic Materials: Strategies to Improve Their Photochromic Properties. *J. Mater. Chem. C* **2018**, *6* (2), 191–212. https://doi.org/10.1039/c7tc04189f.

(2) Zhang, J.; Zou, Q.; Tian, H. Photochromic Materials: More than Meets the Eye. *Adv. Mater.* **2013**, *25* (3), 378–399. https://doi.org/10.1002/adma.201201521.

(3) Pardo, R.; Zayat, M.; Levy, D. Photochromic Organic-Inorganic Hybrid Materials. *Chem. Soc. Rev.* **2011**, *40* (2), 672–687. https://doi.org/10.1039/c0cs00065e.

(4) Nafezarefi, F.; Schreuders, H.; Dam, B.; Cornelius, S. Photochromism of Rare-Earth Metal-Oxy-Hydrides. *Appl. Phys. Lett.* **2017**, *111* (10). https://doi.org/10.1063/1.4995081.

(5) Kobayashi, Y.; Mishima, Y.; Mutoh, K.; Abe, J. Highly Durable Photochromic Radical Complexes Having No Steric Protections of Radicals. *Chem. Commun.* **2017**, *53* (31), 4315–4318. https://doi.org/10.1039/c7cc01439b.

(6) Miyazaki, H.; Matsuura, T.; Ota, T. Nickel Oxide-Based Photochromic Composite Fi Lms. **2016**, 1175–1177.

(7) Yang, Y. A.; Ma, Y.; Yao, J. N.; Loo, B. H. Simulation of the Sublimation Process in the Preparation of Photochromic WO3 Film by Laser Microprobe Mass Spectrometry. *J. Non. Cryst.*

Solids **2000**, *272* (1), 71–74. https://doi.org/10.1016/S0022-3093(00)00226-X.
(8) Xu, N.; Sun, M.; Cao, Y. W.; Yao, J. N.; Wang, E. G. Influence of PH on Structure and Photochromic Behavior of Nanocrystalline WO3 Films. *Appl. Surf. Sci.* **2000**, *157* (1), 81–84. https://doi.org/10.1016/S0169-4332(99)00523-1.
(9) Ikake, H.; Hashimoto, W.; Obara, T.; Kurita, K.; Yano, S. Photochromic Properties and Microstructures of Poly (Tetramethylene Oxide)/Tungsten Trioxide Hybrid Materials. *Kobunshi Ronbunshu* **2000**, *57* (6), 376–382.
(10) Li, S.; Germanenko, I. N.; El-Shall, M. S. Nanoparticles from the Vapor Phase: Synthesis and Characterization of Si, Ge, MoO3, and WO3 Nanocrystals. *J. Clust. Sci.* **1999**, *10* (4), 533–547. https://doi.org/10.1023/A:1021957108775.
(11) Su, L.; Dai, Q.; Lu, Z. Spectroelectrochemical and Photoelectrochemical Studies of Electrodeposited Tungsten Trioxide Films. *Spectrochim. Acta - Part A Mol. Biomol. Spectrosc.* **1999**, *55* (11), 2179–2185. https://doi.org/10.1016/S1386-1425(99)00011-6.
(12) Ajito, K.; Nagahara, L. A.; Tryk, D. A.; Hashimoto, K.; Fujishima, A. Study of the Photochromic Properties of Amorphous MoO3 Films Using Raman Microscopy. *J. Phys. Chem.* **1995**, *99* (44), 16383–16388. https://doi.org/10.1021/j100044a028.
(13) Yao, J. N.; Yang, Y. A.; Loo, B. H. Enhancement of Photochromism and Electrochromism in MoO3/Au and MoO3/Pt Thin Films. *J. Phys. Chem. B* **1998**, *102* (11), 1856–1860. https://doi.org/10.1021/jp972217u.
(14) Loo, B. H.; Yao, J. N.; D., C. H.; Hashimoto, K.; Fujishima, A. A Raman Microprobe Study of the Electrochromic and Photochromic Thin Films of Molybdenum Trioxide and Tungsten Trioxide. *Appl. Surf. Sci.* **1994**, No. 81, 175–181.
(15) Li, N.; Li, Y.; Zhou, Y.; Li, W.; Ji, S.; Yao, H.; Cao, X.; Jin, P. Interfacial-Charge-Transfer-Induced Photochromism of MoO3@TiO2 Crystalline-Core Amorphous-Shell Nanorods. *Sol. Energy Mater. Sol. Cells* **2017**, *160* (September 2016), 116–125. https://doi.org/10.1016/j.solmat.2016.10.016.
(16) Miyazaki, H.; Matsuura, T.; Ota, T. Vanadium Oxide-Based Photochromic Composite Film. *RSC Adv.* **2017**, *7* (5), 2388–2391. https://doi.org/10.1039/c6ra25892a.
(17) Pan, L.; Wang, Y.; Wang, X. J.; Qu, H. Y.; Zhao, J. P.; Li, Y.; Gavrilyuk, A. Hydrogen Photochromism in Nb2O5 Powders. *Phys. Chem. Chem. Phys.* **2014**, *16* (38), 20828–20833. https://doi.org/10.1039/c4cp02834a.
(18) Diop, D. K.; Simonot, L.; Martínez-García, J.; Hébert, M.; Lefkir, Y.; Abadias, G.; Guérin, P.; Babonneau, D.; Destouches, N. Spectral and Color Changes of Ag/TiO2 Photochromic Films Deposited on Diffusing Paper and Transparent Flexible Plastic Substrates. *Appl. Spectrosc.* **2017**, *71* (6), 1271–1279. https://doi.org/10.1177/0003702816680000.
(19) Alcober, C.; Alvarez, F.; Bilmes, S. A.; Candal, R. J. Photochromic W-TiO2 Membranes. *J. Mater. Sci. Lett.* **2002**, *21* (6), 501–504. https://doi.org/10.1023/A:1015399010351.
(20) Wang, S.; Kershaw, S. V.; Li, G.; Leung, M. K. H. The Self-Assembly Synthesis of Tungsten Oxide Quantum Dots with Enhanced Optical Properties. *J. Mater. Chem. C* **2015**, *3* (14), 3280–3285. https://doi.org/10.1039/c5tc00278h.
(21) Fu, H.; Xu, T.; Zhu, S.; Zhu, Y. Photocorrosion Inhibition and Enhancement of Photocatalytic Activity for ZnO via Hybridization with C 60. *Environ. Sci. Technol.* **2008**, *42* (21), 8064–8069. https://doi.org/10.1021/es801484x.
(22) Ali, M.; Winterer, M. ZnO Nanocrystals: Surprisingly “Alive.” *Chem. Mater.* **2010**, *22* (1), 85–91. https://doi.org/10.1021/cm902240c.
(23) Khan, S.; Cho, H.; Kim, D.; Han, S. S.; Lee, K. H.; Cho, S. H.; Song, T.; Choi, H. Defect

Engineering toward Strong Photocatalysis of Nb-Doped Anatase TiO2: Computational Predictions and Experimental Verifications. *Appl. Catal. B Environ.* **2017**, *206*, 520–530. https://doi.org/10.1016/j.apcatb.2017.01.039.
(24) Joost, U.; Šutka, A.; Oja, M.; Smits, K.; Döbelin, N.; Loot, A.; Järvekülg, M.; Hirsimäki, M.; Valden, M.; Nõmmiste, E. Reversible Photodoping of TiO2 Nanoparticles for Photochromic Applications. *Chem. Mater.* **2018**, *30* (24), 8968–8974. https://doi.org/10.1021/acs.chemmater.8b04813.
(25) Renz, C. Lichtreaktionen Der Oxyde Des Titans, Cers Und Der Erdsäuren. *Helv. Chim. Acta* **1921**, *4* (1), 961–968. https://doi.org/10.1002/hlca.192100401101.
(26) Miyazaki, H.; Matsuura, T.; Ota, T. TiO2nano-Particles Based Photochromic Composite Films. *Compos. Commun.* **2018**, *10* (September), 136–139. https://doi.org/10.1016/j.coco.2018.09.004.
(27) Uyen Thi, P. N.; Male, U.; Huh, D. S. Fabrication of Photo-Responsive Moth Eye-like Patterned Poly(Vinyl Alcohol) Films Selectively Containing TiO2nanoparticles in the Microdome. *Polymer (Guildf).* **2018**, *144*, 103–110. https://doi.org/10.1016/j.polymer.2018.04.044.
(28) Nussbaumer, R. J.; Caseri, W. R.; Smith, P. Reversible Photochromic Properties of TiO2-Polymer Nanocomposites. *J. Nanosci. Nanotechnol.* **2006**, *6* (2), 459–463. https://doi.org/10.1166/jnn.2006.923.
(29) Wang, K.; Chen, P.; Nie, W.; Xu, Y.; Zhou, Y. Improved Photocatalytic Reduction of Cr(VI) by Molybdenum Disulfide Modified with Conjugated Polyvinyl Alcohol. *Chem. Eng. J.* **2019**, *359* (October 2018), 1205–1214. https://doi.org/10.1016/j.cej.2018.11.057.
(30) Serpone, N.; Texier, I.; Emeline, A. V.; Pichat, P.; Hidaka, H.; Zhao, J. Post-Irradiation Effect and Reductive Dechlorination of Chlorophenols at Oxygen-Free TiO2/Water Interfaces in the Presence of Prominent Hole Scavengers. *J. Photochem. Photobiol. A Chem.* **2000**, *136* (3), 145–155. https://doi.org/10.1016/S1010-6030(00)00348-8.
(31) Shkrob, I. A.; Sauer, M. C.; Gosztola, D. Efficient, Rapid Photooxidation of Chemisorbed Polyhydroxyl Alcohols and Carbohydrates by TiO 2 Nanoparticles in an Aqueous Solution. *J. Phys. Chem. B* **2004**, *108* (33), 12512–12517. https://doi.org/10.1021/jp0477351.
(32) Uyen Thi, P. N.; Male, U.; Huh, D. S. Fabrication of Photo-Responsive Moth Eye-like Patterned Poly(Vinyl Alcohol) Films Selectively Containing TiO2 Nanoparticles in the Microdome. *Polymer (Guildf).* **2018**, *144*, 103–110. https://doi.org/10.1016/j.polymer.2018.04.044.
(33) Di Valentin, C.; Fittipaldi, D. Hole Scavenging by Organic Adsorbates on the TiO2surface: A DFT Model Study. *J. Phys. Chem. Lett.* **2013**, *4* (11), 1901–1906. https://doi.org/10.1021/jz400624w.
(34) Eglītis, R.; Zukuls, A.; Viter, R.; Šutka, A. Kinetics of TiO2 Photochromic Response in Different Hole Scavenger Solvents. *Photochem. Photobiol. Sci.* **2020**, 1072–1077. https://doi.org/10.1039/d0pp00079e.
(35) Safeen, K.; Micheli, V.; Bartali, R.; Gottardi, G.; Safeen, A.; Ullah, H.; Laidani, N. Synthesis of Conductive and Transparent Nb-Doped TiO2 Films: Role of the Target Material and Sputtering Gas Composition. *Mater. Sci. Semicond. Process.* **2017**, *66* (January), 74–80. https://doi.org/10.1016/j.mssp.2017.04.012.
(36) Manole, A. V.; Dobromir, M.; Gîrtan, M.; Mallet, R.; Rusu, G.; Luca, D. Optical Properties of Nb-Doped TiO2 Thin Films Prepared by Sol–Gel Method. *Ceram. Int.* **2013**, *39* (5), 4771–4776. https://doi.org/10.1016/j.ceramint.2012.11.066.
(37) De Trizio, L.; Buonsanti, R.; Schimpf, A. M.; Llordes, A.; Gamelin, D. R.; Simonutti, R.; Milliron, D. J. Nb-Doped Colloidal TiO 2 Nanocrystals with Tunable Infrared Absorption. *Chem. Mater.* **2013**, *25* (16), 3383–3390. https://doi.org/10.1021/cm402396c.

(38) Koo, B. R.; Oh, D. H.; Ahn, H. J. Influence of Nb-Doped TiO2blocking Layers as a Cascading Band Structure for Enhanced Photovoltaic Properties. *Appl. Surf. Sci.* **2018**, *433*, 27–34. https://doi.org/10.1016/j.apsusc.2017.10.078.
(39) Dahlman, C. J.; Agrawal, A.; Staller, C. M.; Adair, J.; Milliron, D. J. Anisotropic Origins of Localized Surface Plasmon Resonance in N-Type Anatase TiO 2 Nanocrystals. *Chem. Mater.* **2019**, *31* (2), 502–511. https://doi.org/10.1021/acs.chemmater.8b04519.
(40) Panayotov, D. A.; Burrows, S. P.; Morris, J. R. Infrared Spectroscopic Studies of Conduction Band and Trapped Electrons in UV-Photoexcited, H-Atom n-Doped, and Thermally Reduced TiO2. *J. Phys. Chem. C* **2012**, *116* (7), 4535–4544. https://doi.org/10.1021/jp2053103.
(41) Su, H.; Huang, Y. T.; Chang, Y. H.; Zhai, P.; Hau, N. Y.; Cheung, P. C. H.; Yeh, W. T.; Wei, T. C.; Feng, S. P. The Synthesis of Nb-Doped TiO<inf>2</Inf> Nanoparticles for Improved-Performance Dye Sensitized Solar Cells. *Electrochim. Acta* **2015**, *182*, 230–237. https://doi.org/10.1016/j.electacta.2015.09.072.
(42) Kong, L.; Wang, C.; Zheng, H.; Zhang, X.; Liu, Y. Defect-Induced Yellow Color in Nb-Doped TiO<inf>2</Inf> and Its Impact on Visible-Light Photocatalysis. *J. Phys. Chem. C* **2015**, *119* (29), 16623–16632. https://doi.org/10.1021/acs.jpcc.5b03448.
(43) Nikolay, T.; Larina, L.; Shevaleevskiy, O.; Ahn, B. T. Electronic Structure Study of Lightly Nb-Doped TiO2 Electrode for Dye-Sensitized Solar Cells. *Energy Environ. Sci.* **2011**, *4* (4), 1480–1486. https://doi.org/10.1039/c0ee00678e.
(44) Scolan, E.; Sanchez, C. Synthesis and Characterization of Surface-Protected Nanocrystalline Titania Particles. *Chem. Mater.* **1998**, *10* (10), 3217–3223. https://doi.org/10.1021/cm980322q.
(45) Doebelin, N.; Kleeberg, R. Profex: A Graphical User Interface for the Rietveld Refinement Program BGMN. *J. Appl. Crystallogr.* **2015**, *48*, 1573–1580. https://doi.org/10.1107/S1600576715014685.
(46) Schneider, C. A.; Rasband, W. S.; Eliceiri, K. W. NIH Image to ImageJ: 25 Years of Image Analysis. *Nat. Methods* **2012**, *9* (7), 671–675. https://doi.org/10.1038/nmeth.2089.
(47) Schimpf, A. M.; Gunthardt, C. E.; Rinehart, J. D.; Mayer, J. M.; Gamelin, D. R. Controlling Carrier Densities in Photochemically Reduced Colloidal ZnO Nanocrystals: Size Dependence and Role of the Hole Quencher. *J. Am. Chem. Soc.* **2013**, *135* (44), 16569–16577. https://doi.org/10.1021/ja408030u.
(48) Wei, X.; Zhu, G.; Fang, J.; Chen, J. Synthesis , Characterization , and Photocatalysis of Well-Dispersible Phase-Pure Anatase TiO 2 Nanoparticles. **2013**, *2013*.
(49) Mulmi, D. Das; Sekiya, T.; Kamiya, N.; Kurita, S. Optical and Electric Properties of Nb-Doped Anatase TiO 2 Single Crystal.
(50) Zhang, W. F.; He, Y. L.; Zhang, M. S.; Yin, Z.; Chen, Q. Raman Scattering Study on Anatase TiO2 Nanocrystals. *J. Phys. D. Appl. Phys.* **2000**, *33* (8), 912–916. https://doi.org/10.1088/0022-3727/33/8/305.
(51) Singh, S.; Sharma, V.; Sachdev, K. Investigation of Effect of Doping Concentration in Nb-Doped TiO2 Thin Films for TCO Applications. *J. Mater. Sci.* **2017**, *52* (19), 11580–11591. https://doi.org/10.1007/s10853-017-1328-7.
(52) Yang, J.; Zhang, X.; Wang, C.; Sun, P.; Wang, L.; Xia, B.; Liu, Y. Solar Photocatalytic Activities of Porous Nb-Doped TiO 2 Microspheres Prepared by Ultrasonic Spray Pyrolysis. *Solid State Sci.* **2012**, *14* (1), 139–144. https://doi.org/10.1016/j.solidstatesciences.2011.11.010.
(53) Tan, L. L.; Ong, W. J.; Chai, S. P.; Mohamed, A. R. Band Gap Engineered, Oxygen-Rich TiO2 for Visible Light Induced Photocatalytic Reduction of CO2. *Chem. Commun.* **2014**, *50* (52), 6923–6926. https://doi.org/10.1039/c4cc01304b.

(54) Tan, L. L.; Ong, W. J.; Chai, S. P.; Mohamed, A. R. Visible-Light-Activated Oxygen-Rich TiO2 as next Generation Photocatalyst: Importance of Annealing Temperature on the Photoactivity toward Reduction of Carbon Dioxide. *Chem. Eng. J.* **2016**, *283*, 1254–1263. https://doi.org/10.1016/j.cej.2015.07.093.
(55) Parthasarathy, S.; Parthasarathi, V. A Statistical Study on the Measurability of Bijvoet Differences in Crystals with Type-I and Type-II Degree of Centrosymmetry. *Acta Crystallogr. Sect. A* **1976**, *32* (5), 768–771. https://doi.org/10.1107/S0567739476001563.
(56) Yu, N.; Hu, Y.; Wang, X.; Liu, G.; Wang, Z.; Liu, Z.; Tian, Q.; Zhu, M.; Shi, X.; Chen, Z. Dynamically Tuning Near-Infrared-Induced Photothermal Performances of TiO2 Nanocrystals by Nb Doping for Imaging-Guided Photothermal Therapy of Tumors. *Nanoscale* **2017**, *9* (26), 9148–9159. https://doi.org/10.1039/c7nr02180a.
(57) Khan, S.; Cho, H.; Kim, D.; Han, S. S.; Lee, K. H.; Cho, S. H.; Song, T.; Choi, H. Defect Engineering toward Strong Photocatalysis of Nb-Doped Anatase TiO2: Computational Predictions and Experimental Verifications. *Appl. Catal. B Environ.* **2017**, *206*, 520–530. https://doi.org/10.1016/j.apcatb.2017.01.039.
(58) Pan, X.; Yang, M.-Q.; Fu, X.; Zhang, N.; Xu, Y.-J. Defective TiO2 with Oxygen Vacancies: Synthesis, Properties and Photocatalytic Applications. *Nanoscale* **2013**, *5* (9), 3601. https://doi.org/10.1039/c3nr00476g.
(59) Nowotny, M. K.; Sheppard, L. R.; Bak, T.; Nowotny, J. Defect Chemistry of Titanium Dioxide. Application of Defect Engineering in Processing of TiO2-Based Photocatalysts. *J. Phys. Chem. C* **2008**, *112* (14), 5275–5300. https://doi.org/10.1021/jp077275m.
(60) Bharti, B.; Kumar, S.; Lee, H. N.; Kumar, R. Formation of Oxygen Vacancies and Ti 3+ State in TiO 2 Thin Film and Enhanced Optical Properties by Air Plasma Treatment. *Sci. Rep.* **2016**, *6* (August), 1–12. https://doi.org/10.1038/srep32355.
(61) Kutty, T. R. N.; Avudaithai, M. Sacrificial Water Photocleavage Using Nb-Doped TiO2 Fine Particles under Band Gap Irradiation. *Int. J. Hydrogen Energy* **1990**, *15* (9), 621–628. https://doi.org/10.1016/0360-3199(90)90141-K.
(62) Rahimi Niaraki, A.; Saraee, M. R.; Kazemi, F.; Kaboudin, B. Chemoselective Photocatalytic Oxidation of Alcohols to Aldehydes and Ketones by Nitromethane on Titanium Dioxide under Violet 400 Nm LED Light Irradiation. *Org. Biomol. Chem.* **2020**, *18* (12), 2326–2330. https://doi.org/10.1039/c9ob02183c.
(63) Yan, Y.; Han, M.; Konkin, A.; Koppe, T.; Wang, D.; Andreu, T.; Chen, G.; Vetter, U.; Morante, J. R.; Schaaf, P. Slightly Hydrogenated TiO2 with Enhanced Photocatalytic Performance. *J. Mater. Chem. A* **2014**, *2* (32), 12708–12716. https://doi.org/10.1039/c4ta02192d.

SUPPLEMENTARY INFORMATION

Strong, Rapid and Reversible Photochromic Response of Nb doped TiO_2 Nanocrystal Colloids in Hole Scavenging Media

Raivis Eglītis,[a] Urmas Joost,[b] Anzelms Zukuls,[a] Kristaps Rubenis,[c] Reinis Ignatāns,[d] Līga Avotiņa,[e] Larisa Baumane,[f] Krisjānis Šmits,[g] Mika Hirsimäki,[h] Tanel Käämbre,[a,b] Andris Šutka [a,b*]

[a] Research Laboratory of Functional Materials Technologies, Faculty of Materials Science and Applied Chemistry, Riga Technical University, Paula Valdena 3/7, Riga, LV-1048, Latvia

[b] Institute of Physics, University of Tartu, W. Ostwaldi Street 1, Tartu, EE-50411, Estonia

[c] Rudolfs Cimdins Riga Biomaterials Innovations and Development Centre of RTU, Institute of General Chemical Engineering, Faculty of Materials Science, Riga Technical University, Pulka 3, Riga, LV-1007, Latvia

[d] Institute of Materials, École polytechnique fédérale de Lausanne, Lausanne, CH-1015, Switzerland

[e] Institute of Chemical Physics, University of Latvia, Jelgavas street 1, Riga, LV-1586, Latvia

[f] Latvian Institute of Organic Synthesis, Aizkraukles street 21, Riga, LV-1006, Latvia

[g] Institute of Solid State Physics, University of Latvia, Kengaraga street 8, Riga, LV-1063, Latvia

[h] Surface Science Group, Faculty of Engineering and Natural Sciences, Tampere University, P.O. BOX 692, FI-33014 Tampere, Finland

Corresponding author: andris.sutka@rtu.lv

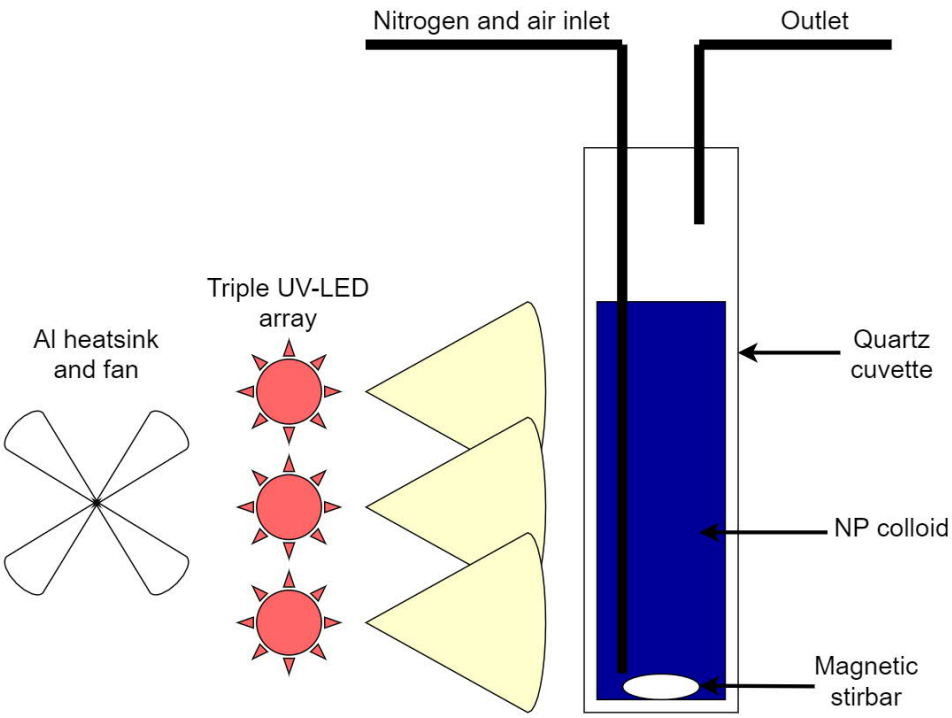

Figure S1. Experimental setup for the determination of photochromic performance. Distance between UV-LEDs and the cuvette – 2.5 cm. LED output power – 15 mW/cm^2.

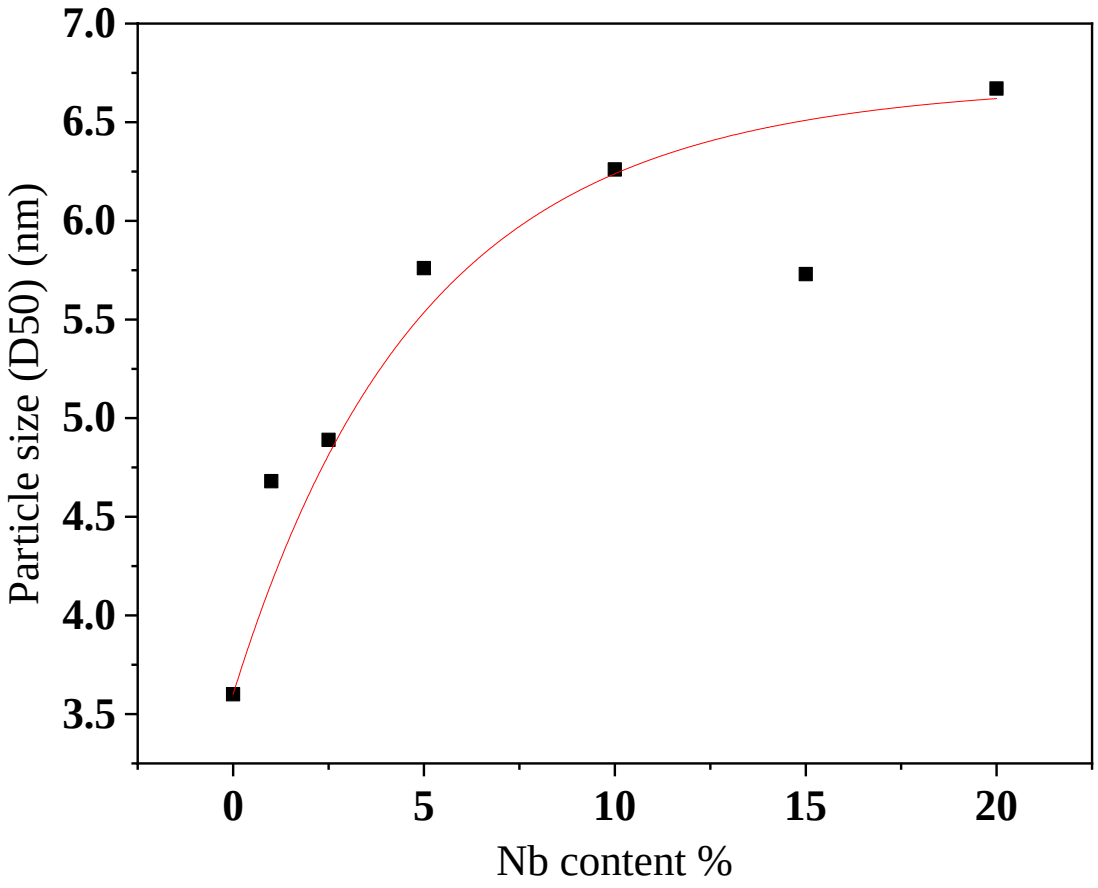

Figure.S2. Particle size d50 (nm) plotted against Nb^{5+} content. The red line indicates a exponential fit for reference.

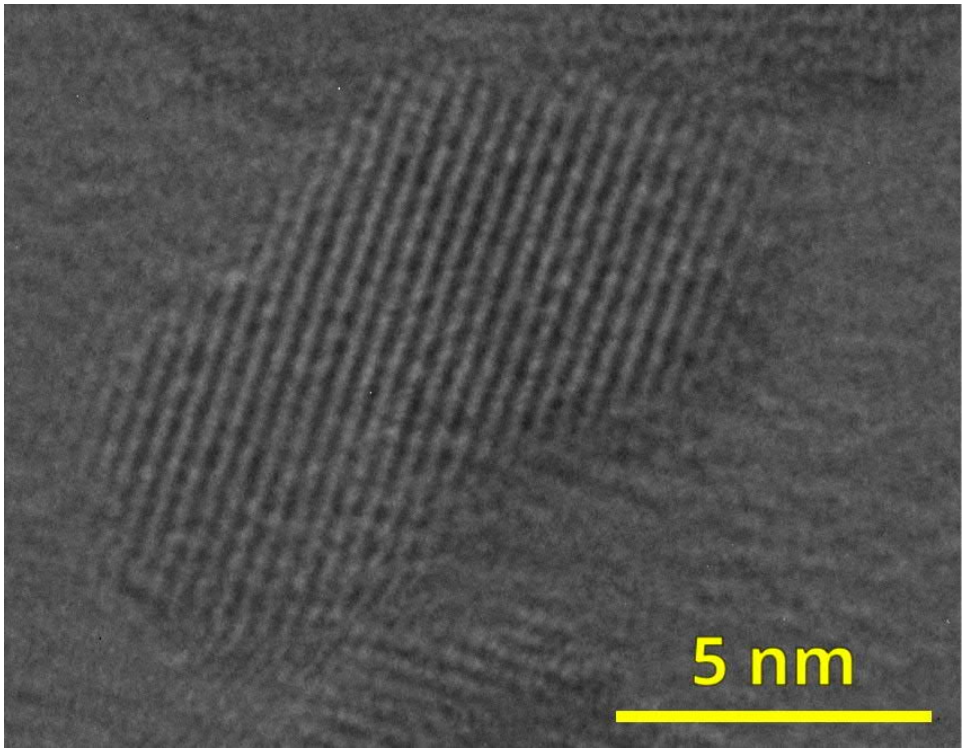

Figure S3. HR-TEM picture of a single Nb-doped TiO_2 nanoparticle.

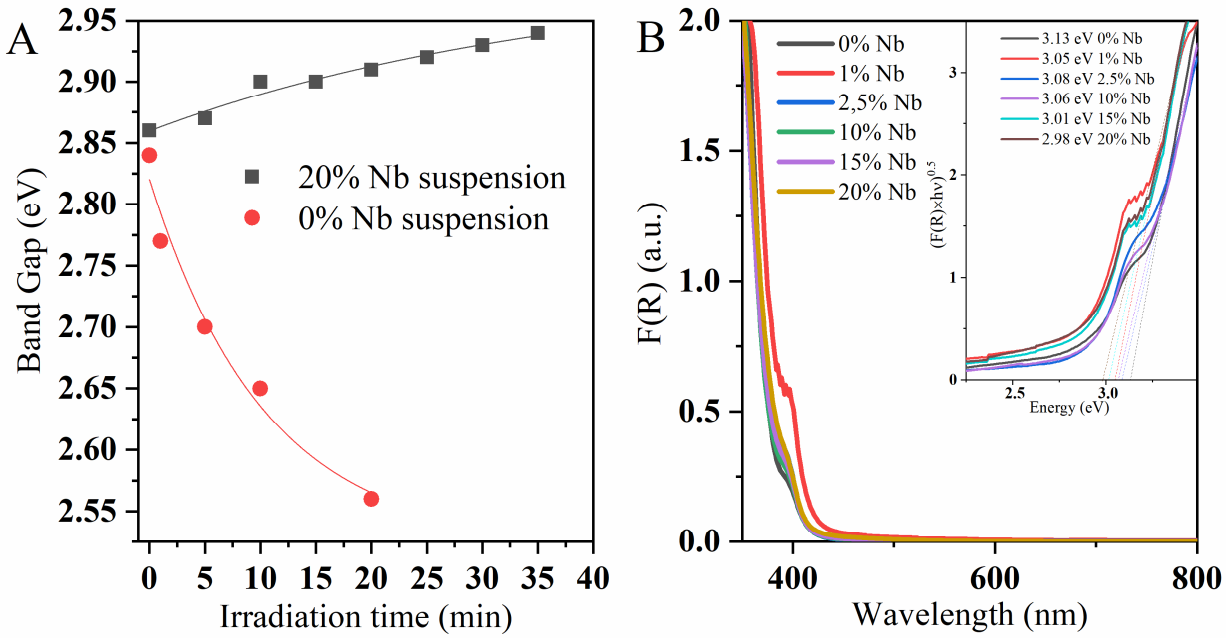

Figure S4. A) Bang gap change during UV irradiation for un-doped TiO_2 NC colloids and 20% Nb TiO_2 NC colloid; B) Kubelka-Munk plots as well as band gap plots for powdered TiO_2 samples with different Nb content.

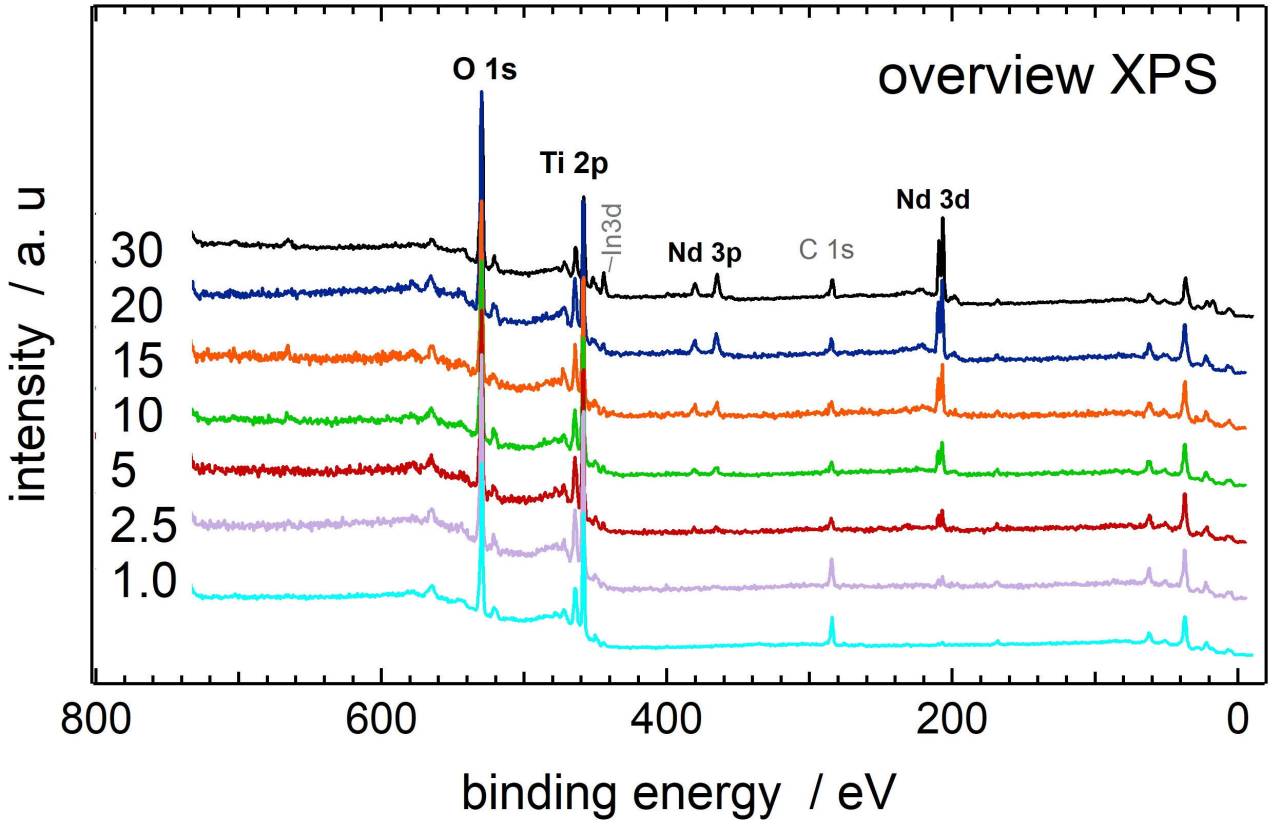

Figure S5. Overview XPS spectra of the Nb-doped TiO_2 NPs

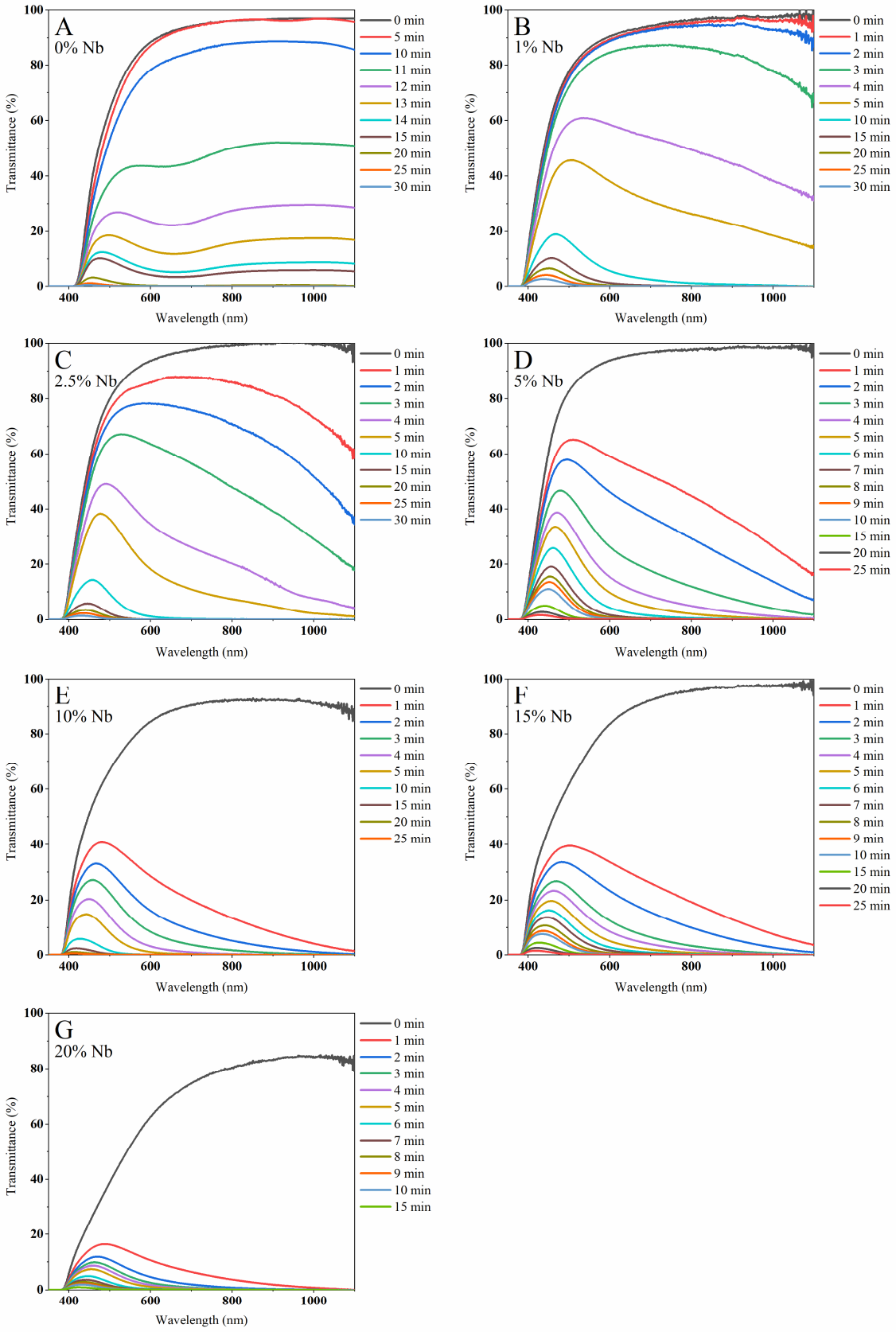

Figure.S6. Transmittance spectra for colloids with a particle content of 100 g/L during UV irradiation. A) un-doped TiO_2; B) 1% Nb; C) 2.5% Nb; D) 5% Nb; E) 10% Nb; F) 15% Nb; G) 20% Nb.

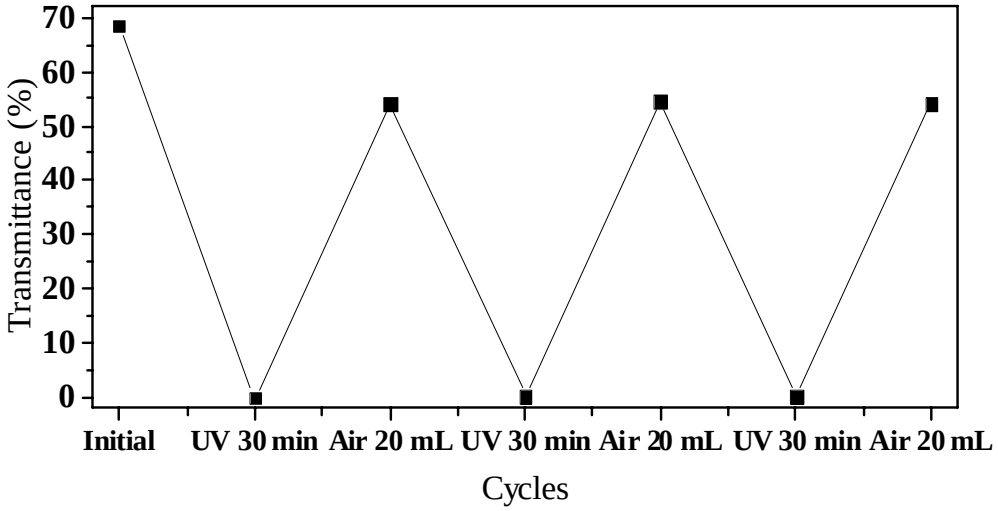

Figure.S7. Repeatability testing done when cycling between UV irradiation and recovery with air injection for the sample with 1% Nb (100 g/L) at a wavelength of 550 nm.

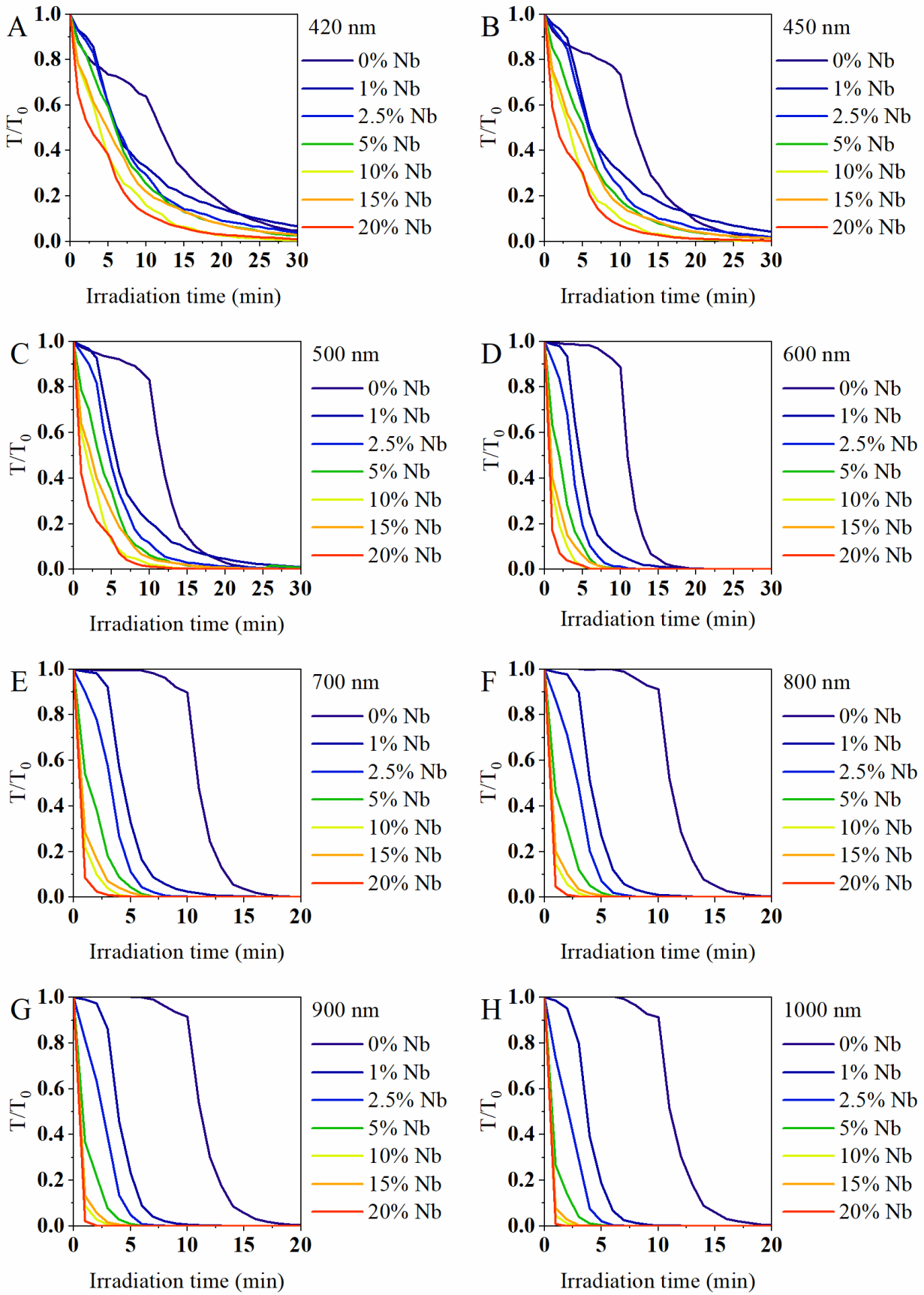

Figure.S8. T/T_0 plots during UV irradiation for samples with different amounts of Nb at A) 420 nm; B) 450 nm; C) 500 nm; D) 600 nm; E) 700 nm; F) 800 nm; G) 900 nm; H) 1000 nm.

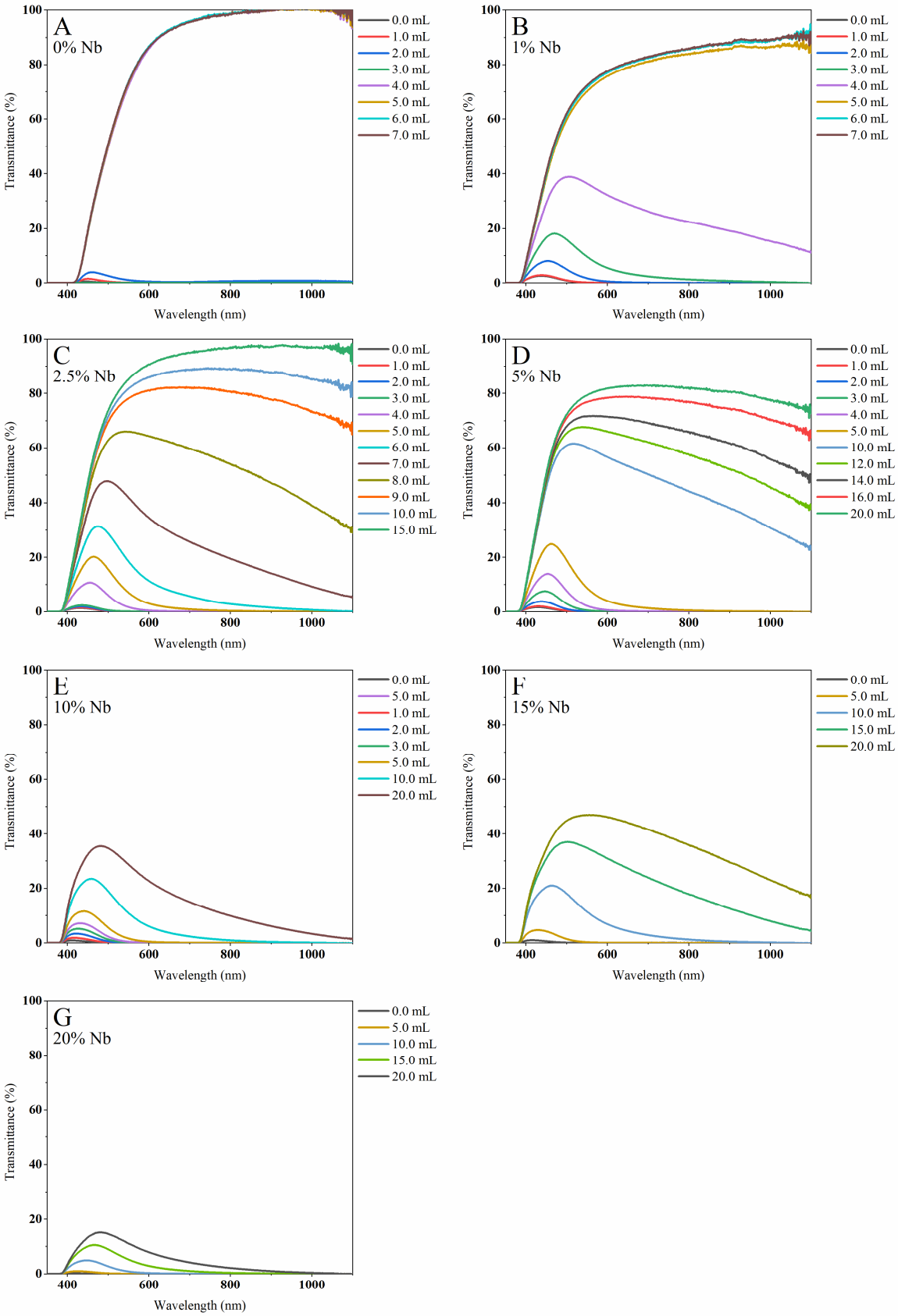

Figure.S9. Transmittance spectra for colloids with a particle content of 100 g/L during dynamic recovery with air injection. A) un-doped TiO_2; B) 1% Nb; C) 2.5% Nb; D) 5% Nb; E) 10% Nb; F) 15% Nb; G) 20% Nb.

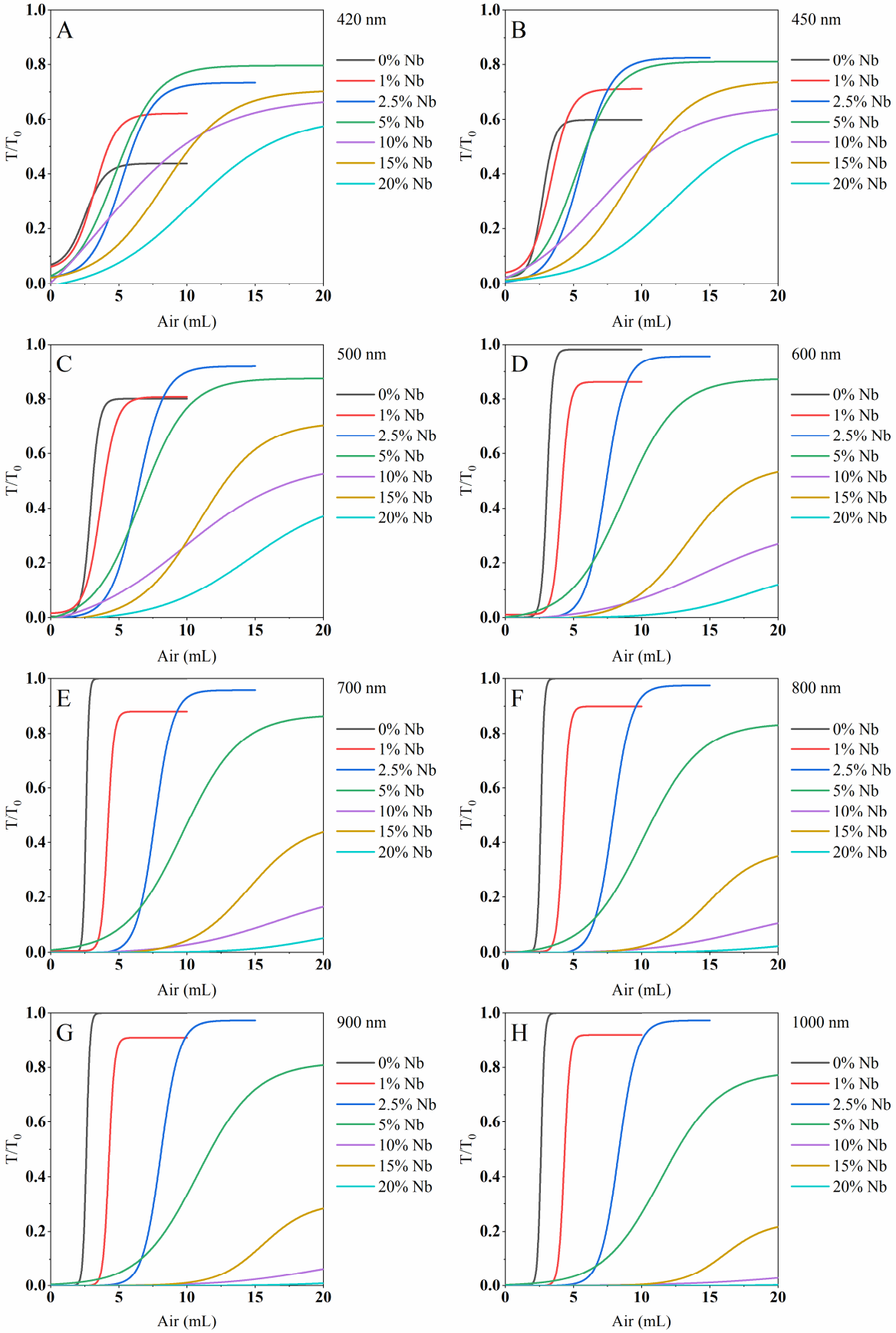

Figure.S10. T/T_0 plots during dynamic recovery for samples with different amounts of Nb at A) 420 nm; B) 450 nm; C) 500 nm; D) 600 nm; E) 700 nm; F) 800 nm; G) 900 nm; H) 1000 nm.

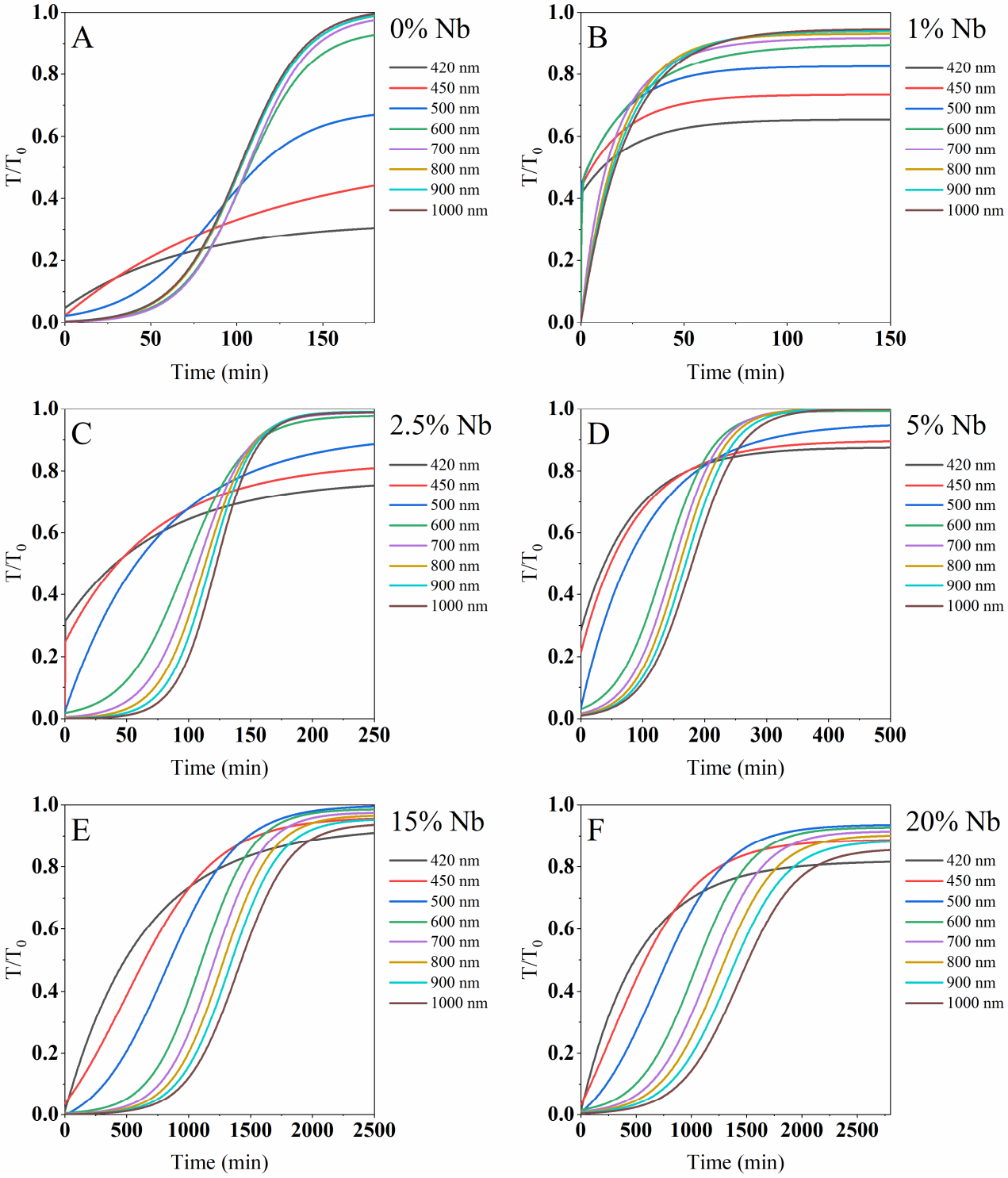

Figure.S11. T/T_0 plots during static recovery at different wavelengths for samples with different Nb content: A) 0% Nb; B) 1% Nb; C) 2.5% Nb; D) 5% Nb; E) 15% Nb; F) 20% Nb.

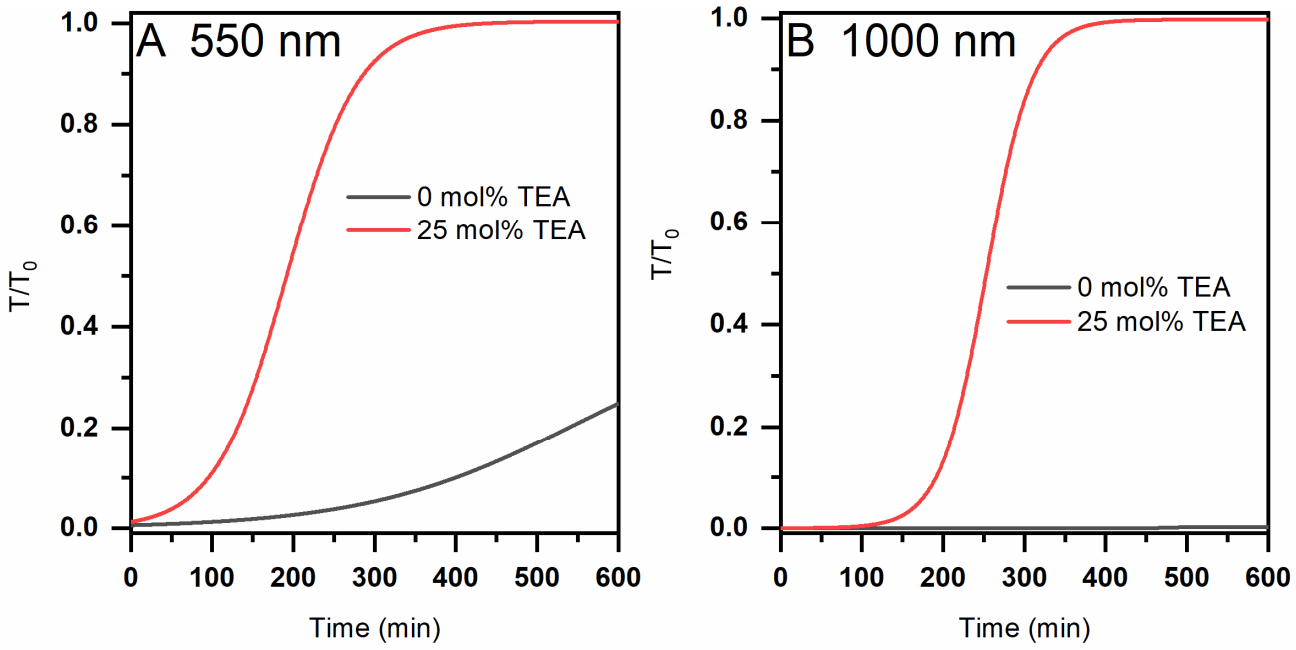

Figure.S12. T/T_0 recovery plots for the colloid of 20% Nb-doped TiO_2 with the addition of 25 mol% of triethanolamine in the absence of air (red curve) and for the colloid without TEA by injecting 5 ml of air (black curve) at 550 nm (A) 1000 nm (B).

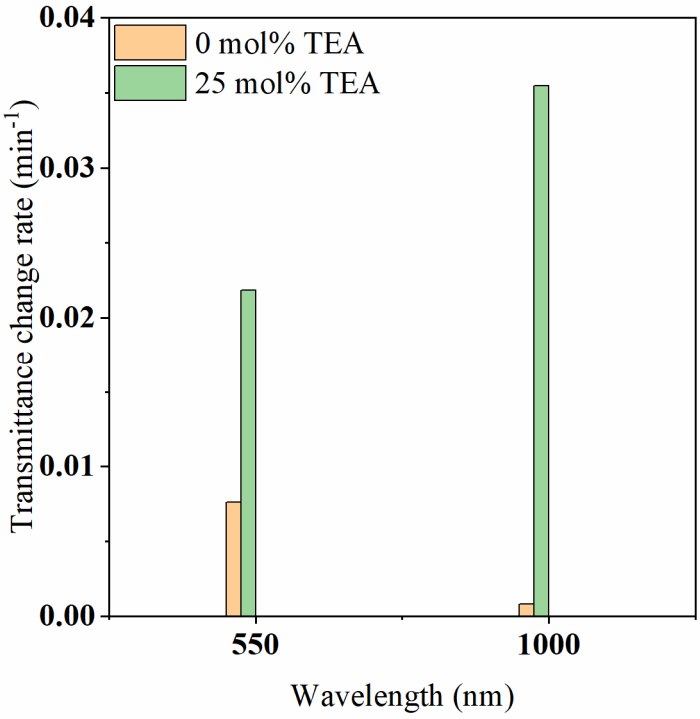

Figure.S13. Transmittance recovery rate constants for the colloid of 20% Nb-doped TiO_2 with the addition of 25 mol% of triethanolamine in the absence of air and for the colloid without TEA by injecting 5 ml of air at 550 nm and 1000 nm.

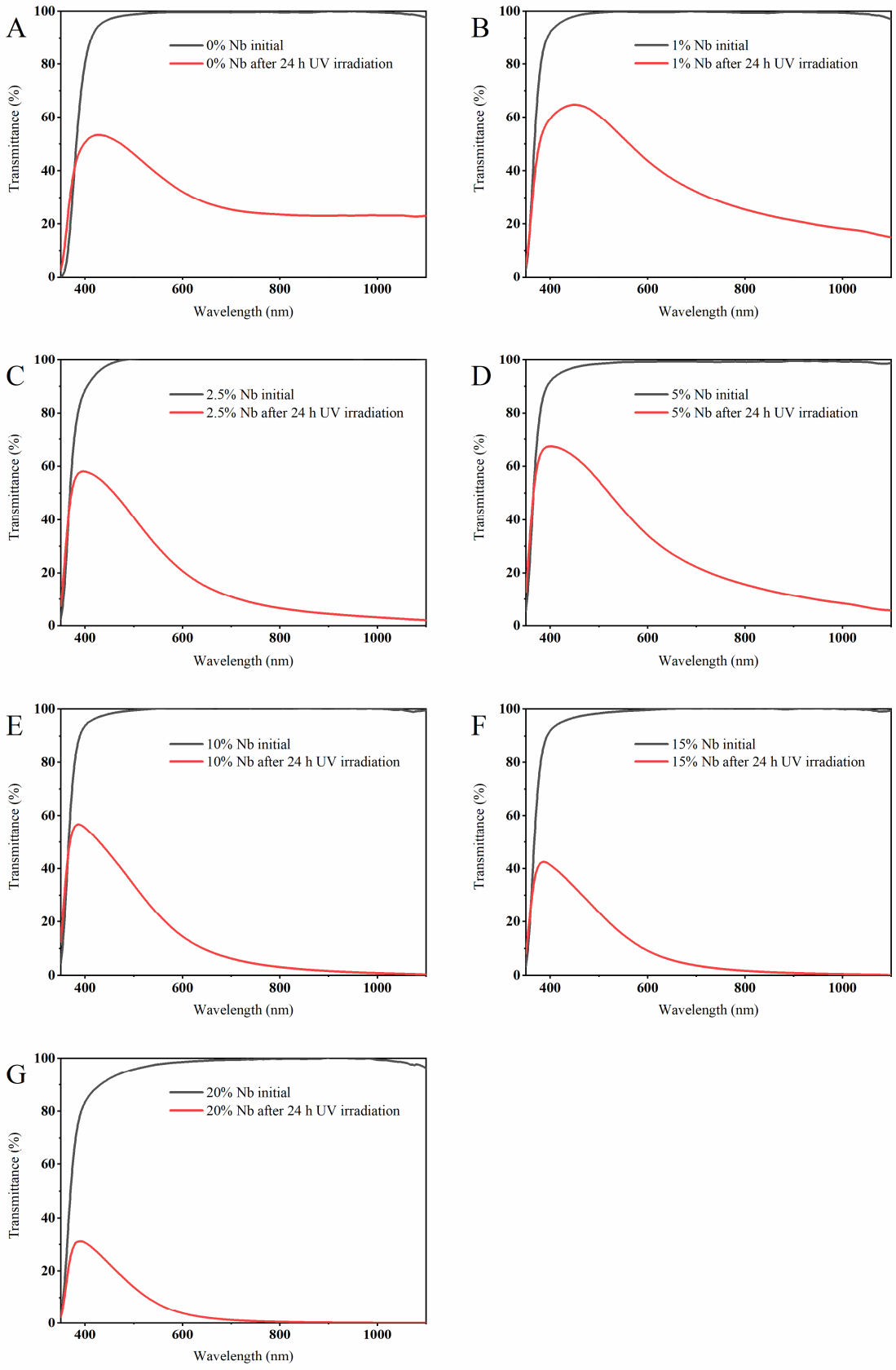

Figure.S14. Transmittance plots for diluted colloids (2 g/L) before and after 24 h UV irradiation for samples with different Nb content: A) 0% Nb; B) 1% Nb; C) 2.5% Nb; D) 5% Nb; E) 15% Nb; F) 20% Nb.

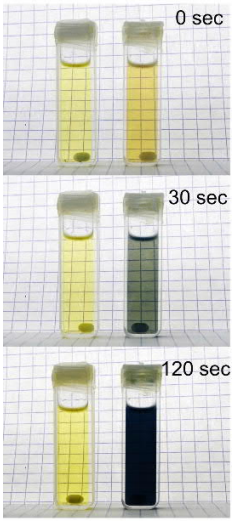

Rapid, strong and reversible photochromic effect is demonstrated in Nb-doped TiO_2 nanoparticle suspensions in hole scavenging medium. The rapid onset and efficiency of light absorption in IR-VIS-UV regime is attributed to collective electronic excitations on the nanoparticles and Nb-induced defects in the TiO_2 matrix.

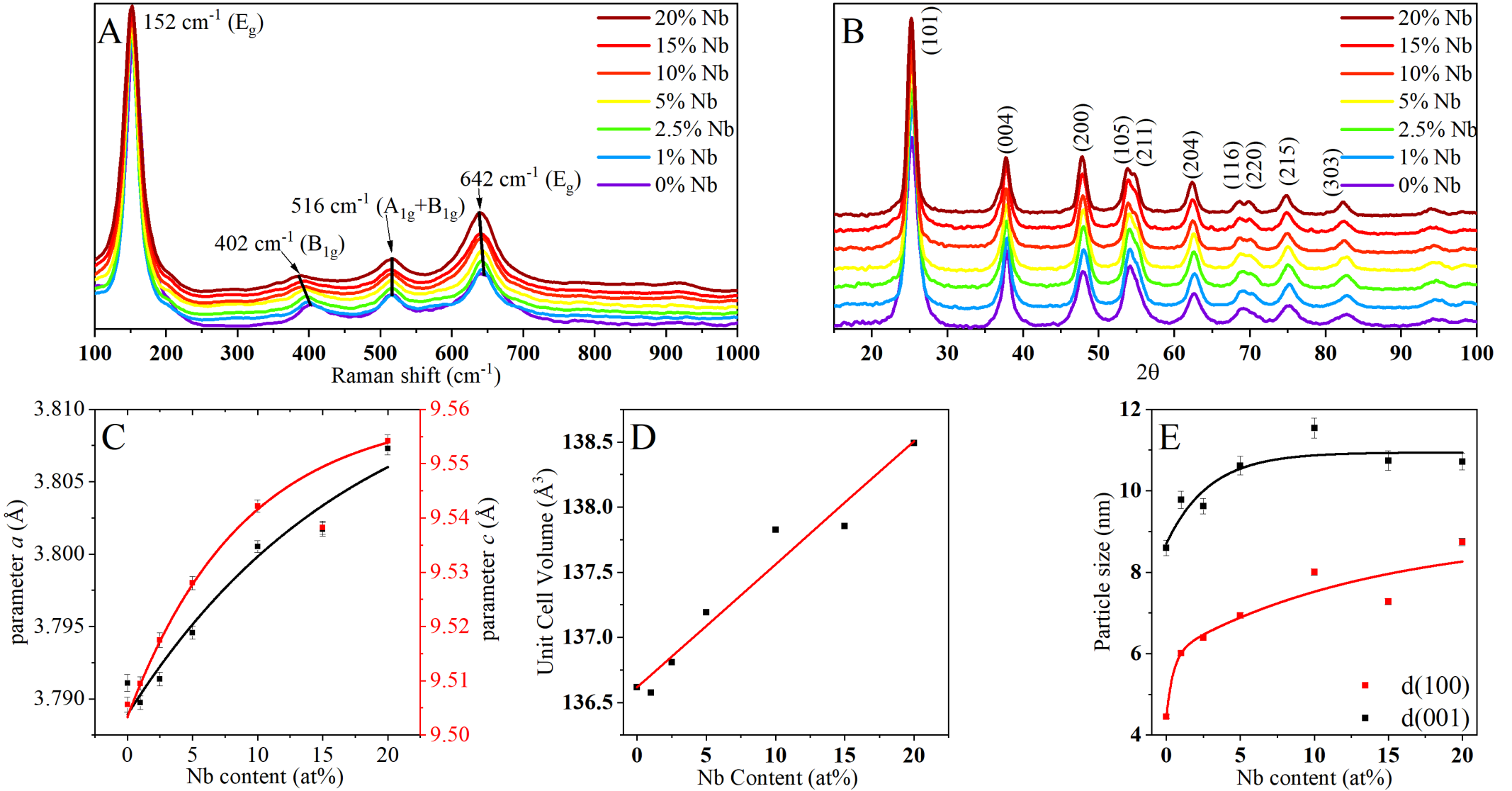
A
152 cm-1 (Eg)
516 cm-1 (A1g+B1g)
642 cm-1 (Eg)
402 cm-1 (B1g)
20% Nb
15% Nb
10% Nb
5% Nb
2.5% Nb
1% Nb
0% Nb
Raman shift (cm-1)
B
(101)
(004)
(200)
(105)
(211)
(204)
(116)
(220)
(215)
(303)
2θ
C
parameter a (Å)
parameter c (Å)
Nb content (at%)
D
Unit Cell Volume (Å3)
Nb Content (at%)
E
Particle size (nm)
d(100)
d(001)
Nb content (at%)

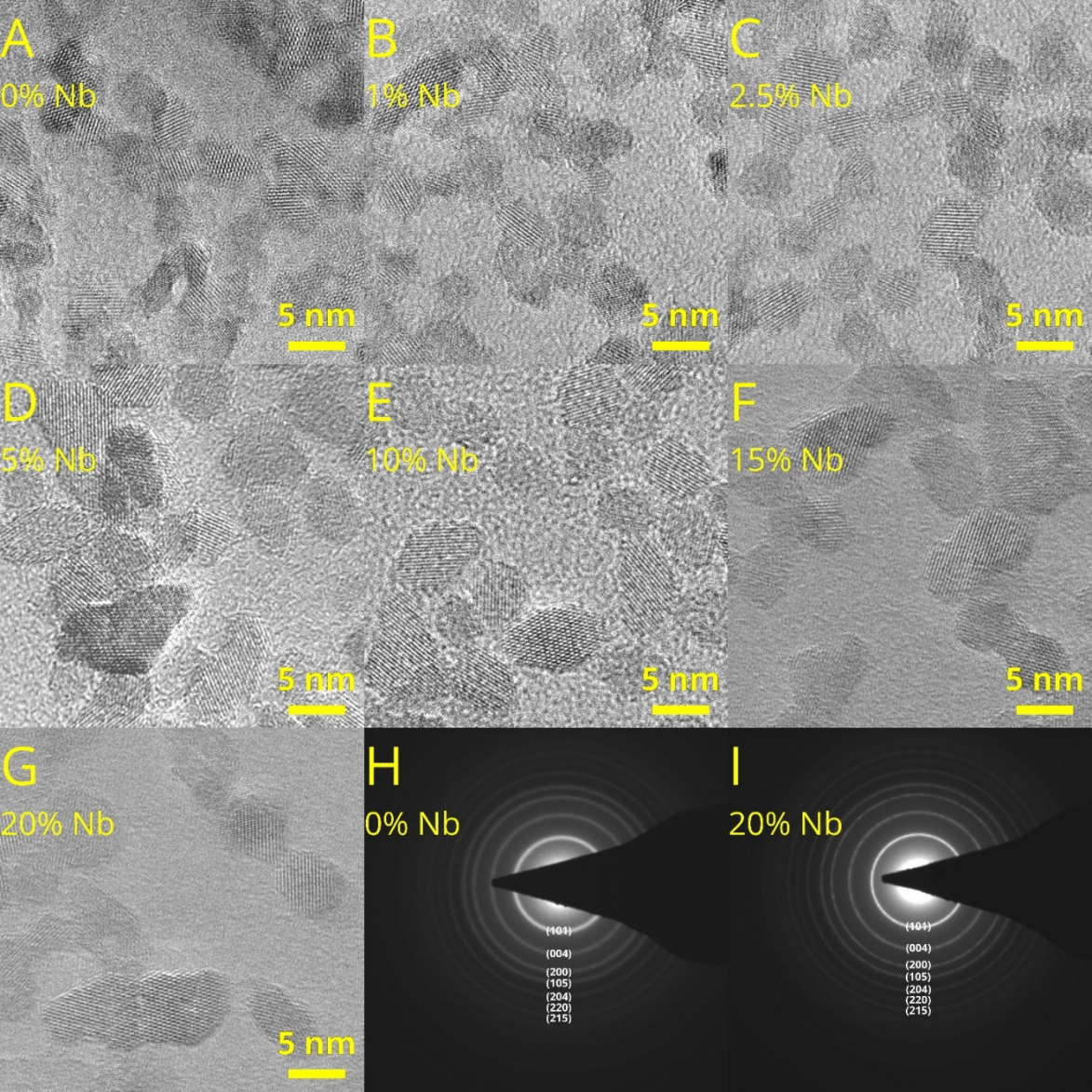
A
0% Nb
5 nm
B
1% Nb
5 nm
C
2.5% Nb
5 nm
D
5% Nb
5 nm
E
10% Nb
5 nm
F
15% Nb
5 nm
G
20% Nb
5 nm
H
0% Nb
(101)
(004)
(200)
(105)
(204)
(220)
(215)
I
20% Nb
(101)
(004)
(200)
(105)
(204)
(220)
(215)

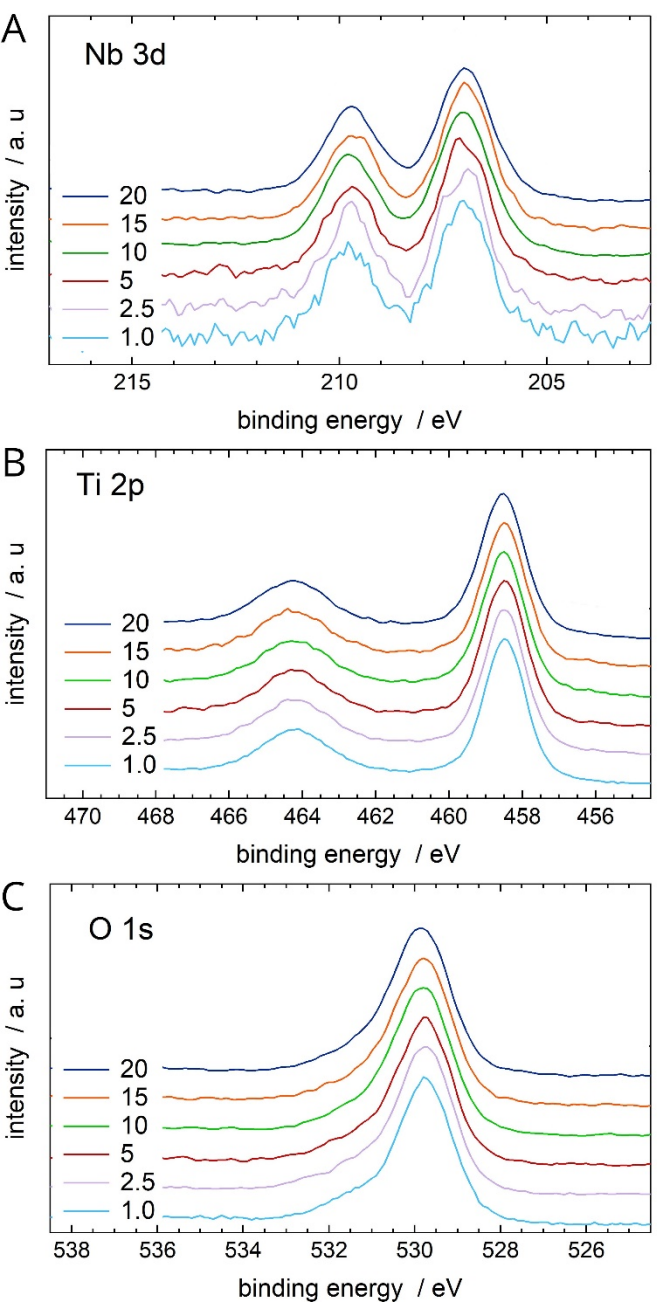
A
Nb 3d
intensity / a. u
20
15
10
5
2.5
1.0
215
210
205
binding energy / eV
B
Ti 2p
intensity / a. u
20
15
10
5
2.5
1.0
470
468
466
464
462
460
458
456
binding energy / eV
C
O 1s
intensity / a. u
20
15
10
5
2.5
1.0
538
536
534
532
530
528
526
binding energy / eV

A

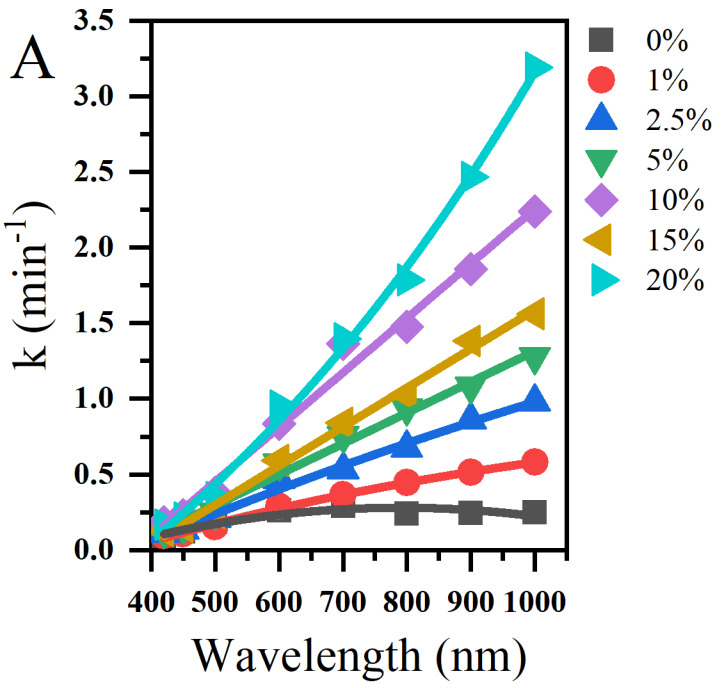
k (min-1)
Wavelength (nm)
0%
1%
2.5%
5%
10%
15%
20%

B

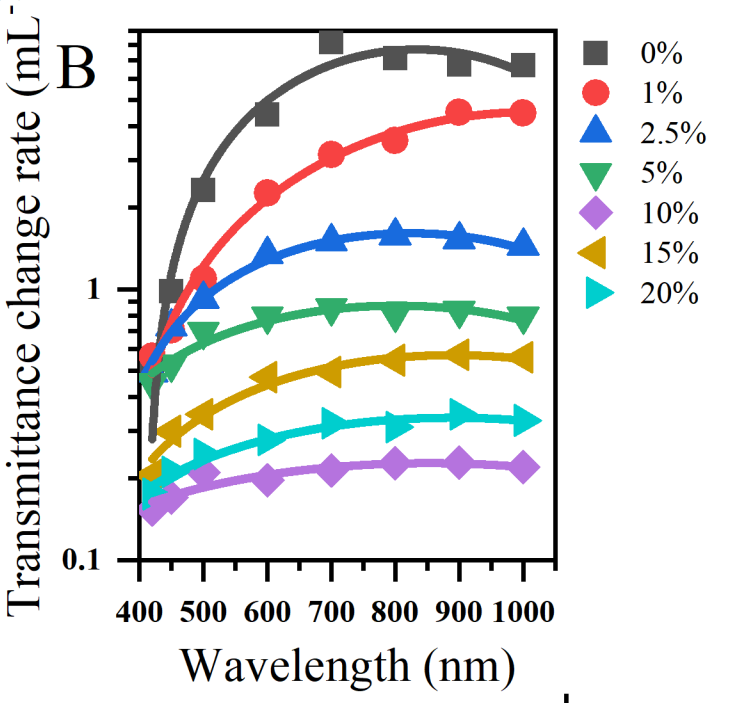
Transmittance change rate (mL-1)
Wavelength (nm)
0%
1%
2.5%
5%
10%
15%
20%

C

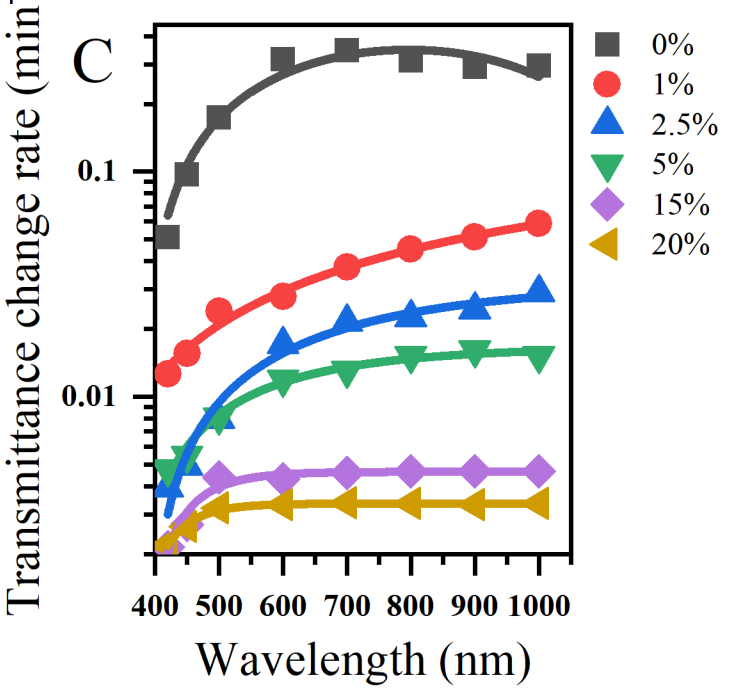
Transmittance change rate (min-1)
Wavelength (nm)
0%
1%
2.5%
5%
15%
20%

D

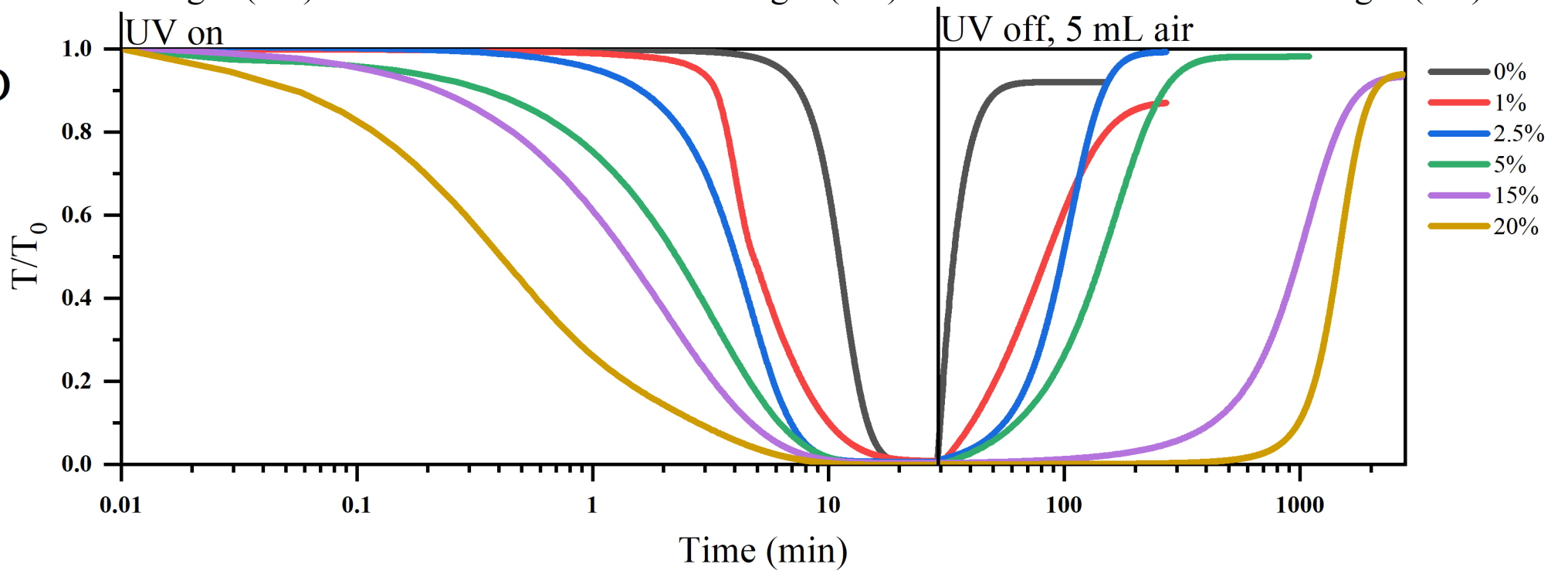
UV on
UV off, 5 mL air
T/T0
Time (min)
0%
1%
2.5%
5%
15%
20%

E

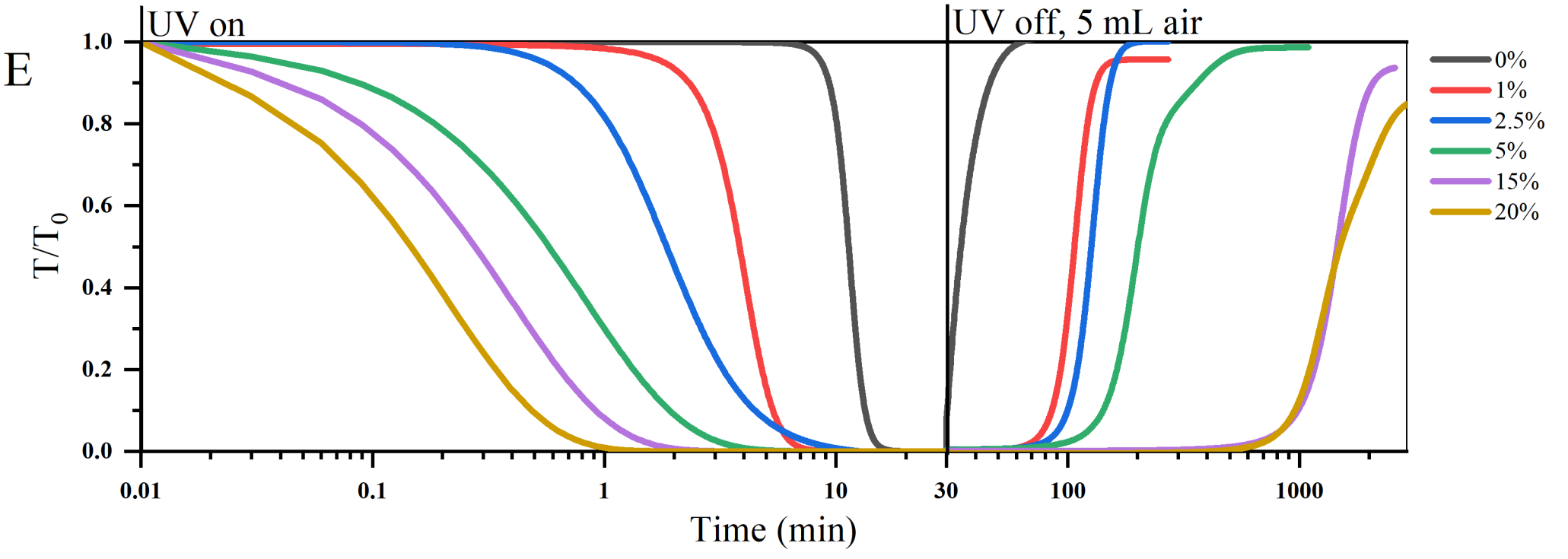
UV on
UV off, 5 mL air
T/T0
Time (min)
0%
1%
2.5%
5%
15%
20%

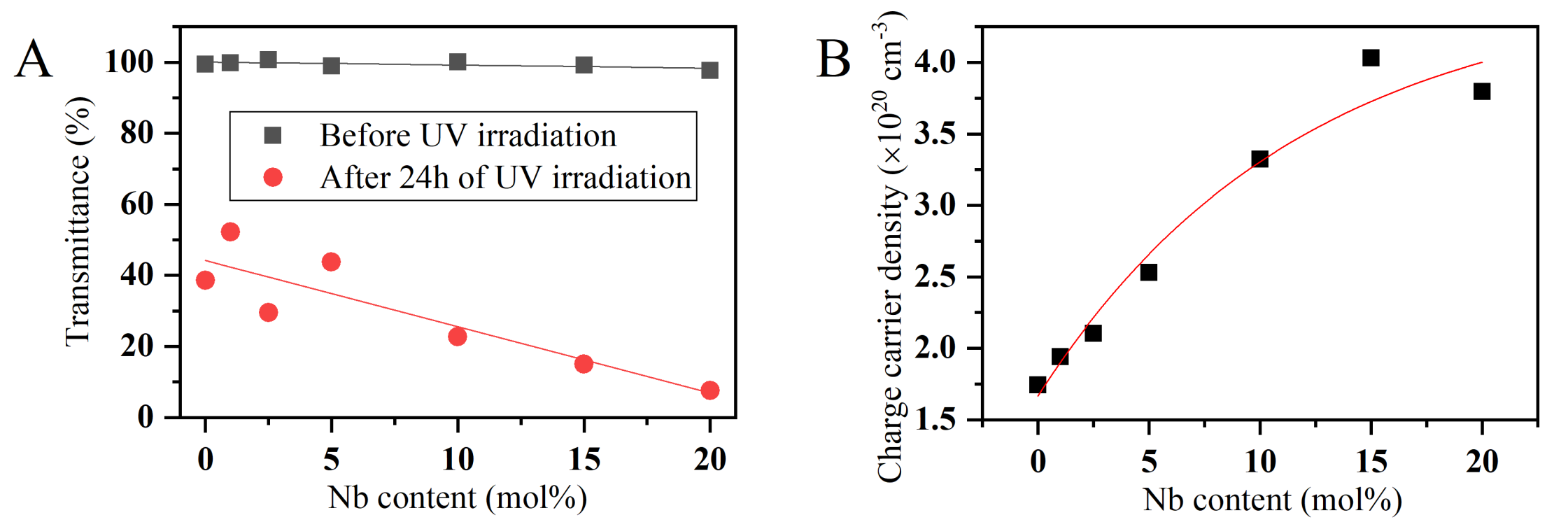
A
Transmittance (%)
100
80
60
40
20
0
Before UV irradiation
After 24h of UV irradiation
0
5
10
15
20
Nb content (mol%)
B
Charge carrier density (×10^20 cm^-3)
4.0
3.5
3.0
2.5
2.0
1.5
0
5
10
15
20
Nb content (mol%)

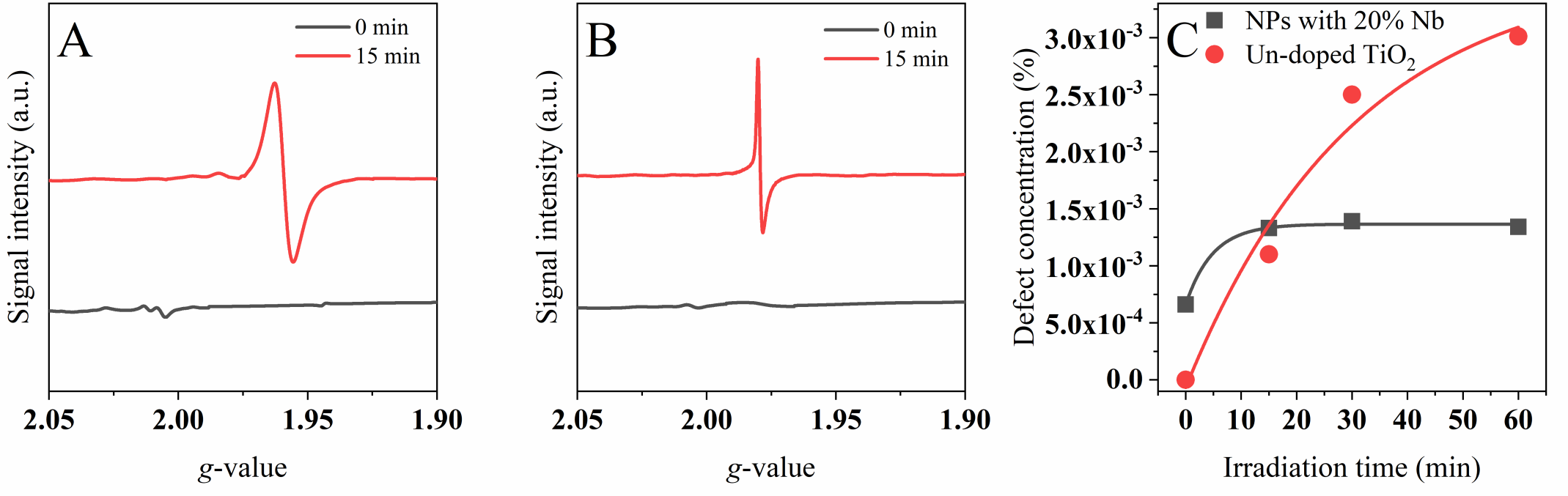
A
0 min
15 min
Signal intensity (a.u.)
2.05
2.00
1.95
1.90
g-value
B
0 min
15 min
Signal intensity (a.u.)
2.05
2.00
1.95
1.90
g-value
C
NPs with 20% Nb
Un-doped TiO2
Defect concentration (%)
3.0x10-3
2.5x10-3
2.0x10-3
1.5x10-3
1.0x10-3
5.0x10-4
0.0
0
10
20
30
40
50
60
Irradiation time (min)

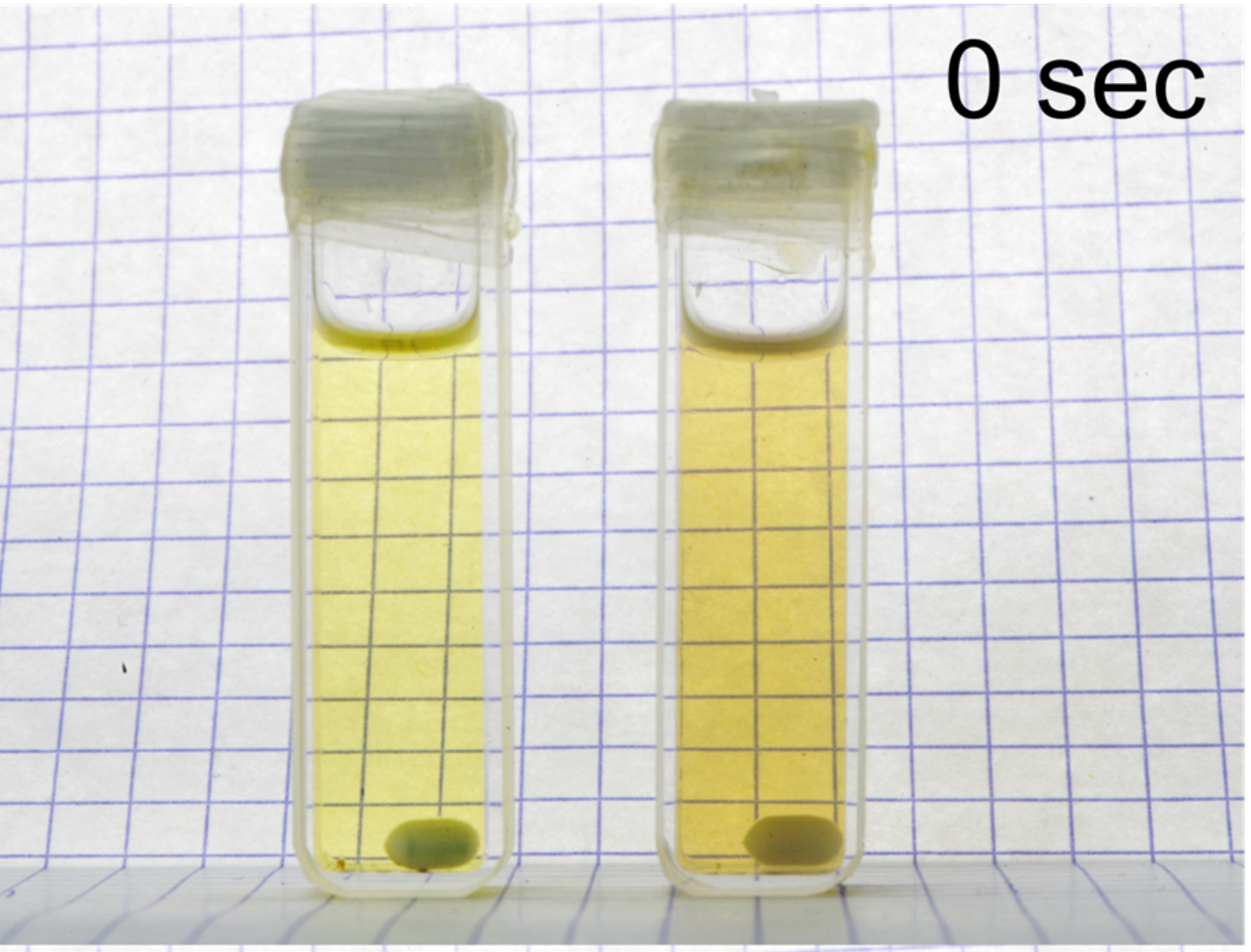
0 sec

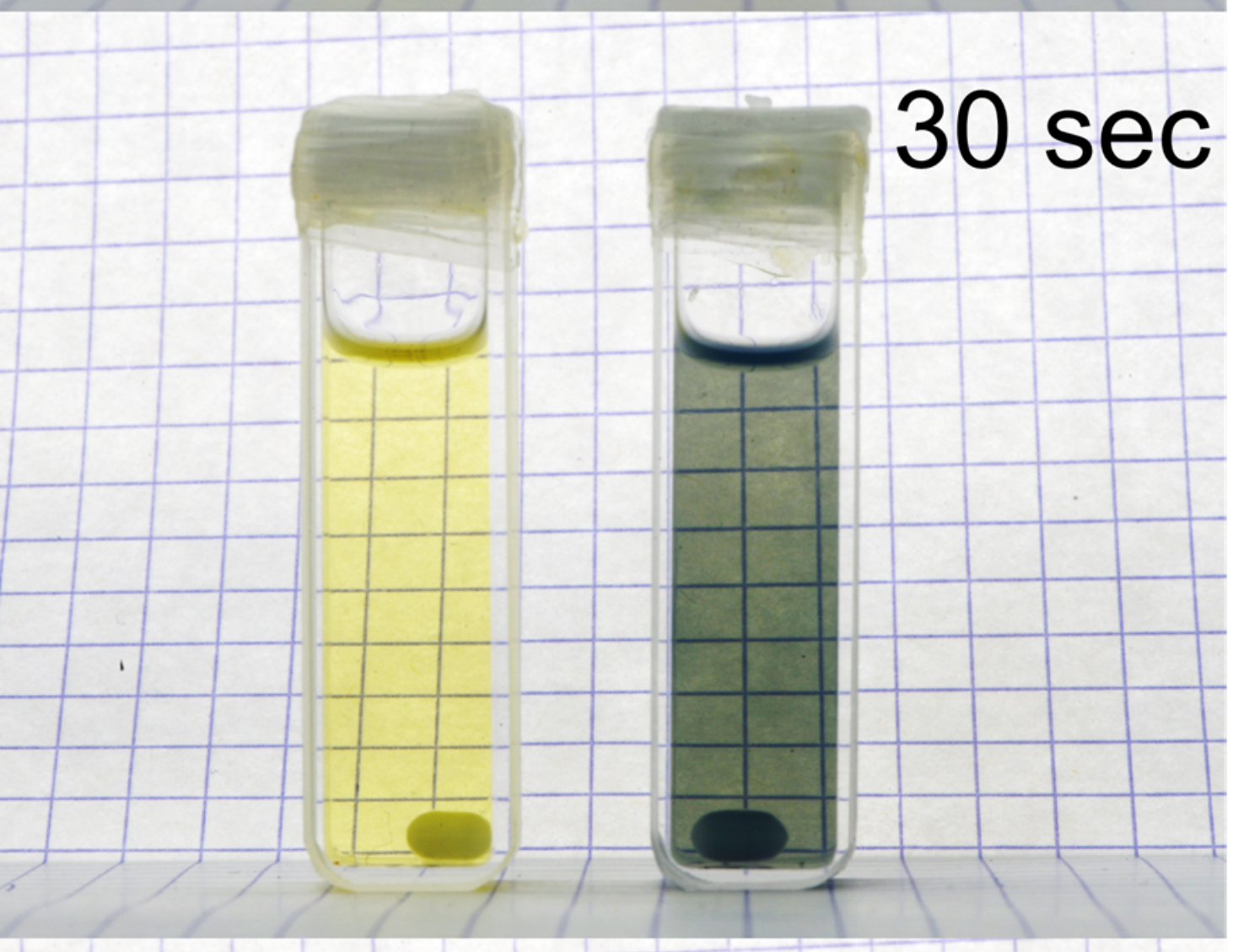
30 sec

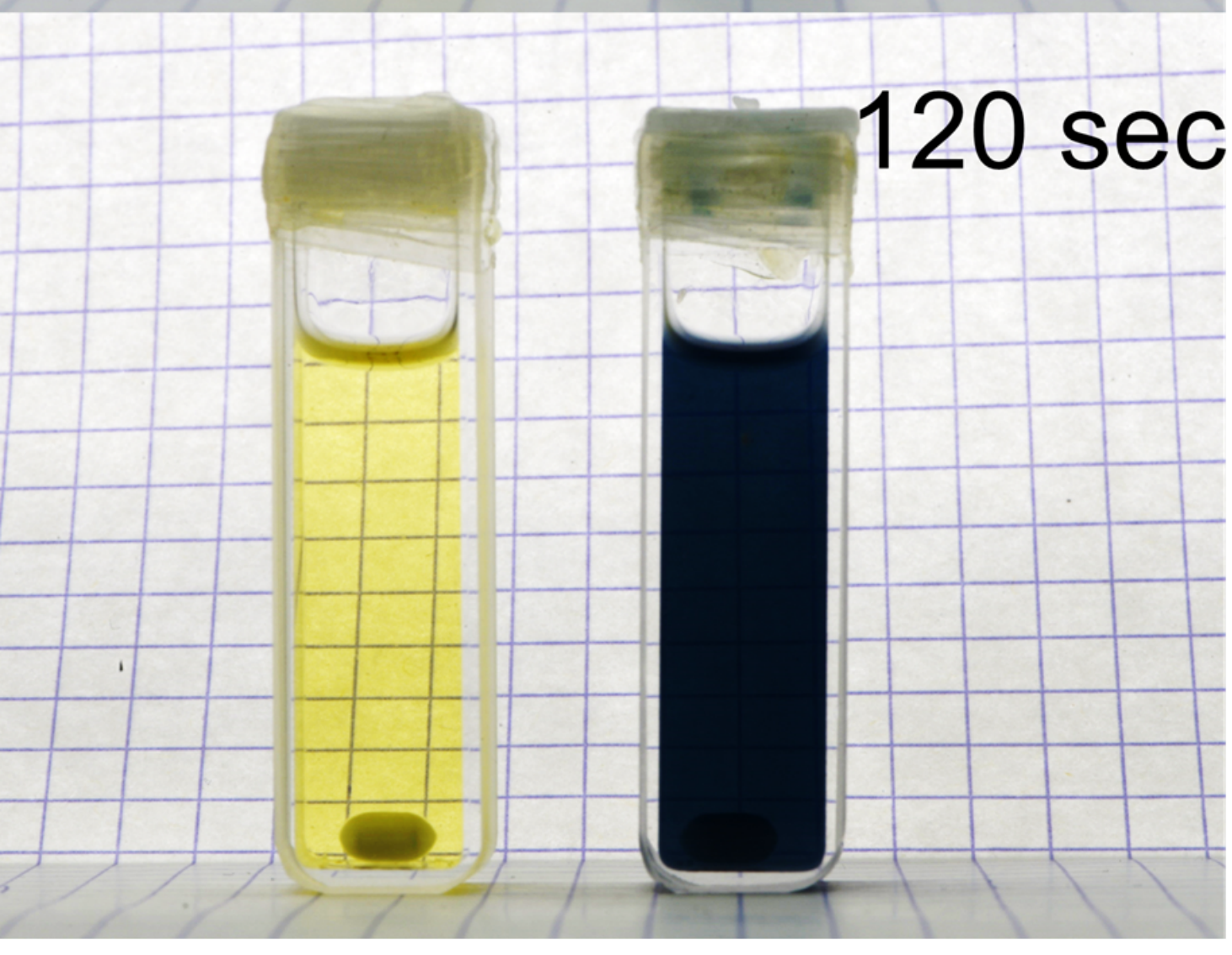
120 sec